nature communications

Article

https://doi.org/10.1038/s41467-025-61114-4

Budesonide-incorporated inhalable lipid nanoparticles for antiTSLP nanobody mRNA delivery to treat steroid-resistant asthma

Received: 17 December 2024

Accepted: 13 June 2025

Published online: 01 July 2025

Check for updates

Jia Huang[1,2], Xin Bai[1,2], William Stewart[3,4], Xiaoyang Xu[3,4] ✉ & Xue-Qing Zhang[1,2] ✉

Asthma exacerbations and steroid resistance occur due to disruption of the airway epithelium, limiting the effectiveness of corticosteroids. Although monoclonal antibodies have progressively emerged as adjunctive therapy for steroid-resistant asthma, there remains a clinical need for targeted anti-inflammatory therapies with better efficacy and fewer off-target effects. Here, we propose the ASCEND (**A**lternative **S**teroids **C**o-delivering with mRNA **E**ncoding **N**anobo**d**ies) approach, which utilizes inhalable lipid nanoparticles formulated with budesonide ($iLNP_{BUD5}$) to deliver mRNA encoding a thymic stromal lymphopoietin nanobody (mnbTSLP) for the treatment of steroid-resistant asthma. Upon nebulization, mnbTSLP-$iLNP_{BUD5}$ targets the lungs, enhancing antiTSLP nanobody production while delivering budesonide. This combined therapy reduces airway inflammation, remodeling, and hyperresponsiveness in murine models. Additionally, mnbTSLP restores the sensitivity of steroid-resistant asthmatic mice to budesonide by inhibiting key inflammatory pathways. The ASCEND approach shows superior effects compared to corticosteroid or antiTSLP antibody treatments, offering a promising strategy for steroid-resistant asthma and potentially other respiratory diseases.

Severe asthma is a persistent and recurrent condition characterized by complex pulmonary inflammation, goblet cell metaplasia, and smooth muscle hypertrophy, causing extensive damage to the airway epithelium, significant impairment of respiratory capacity, and an increased risk of life-threatening complications[1–3]. In many patients, standard corticosteroid therapy attenuates asthma symptoms by binding to intracellular glucocorticoid receptors (GRs), forming a GR complex that translocates to the nucleus, where it activates the downregulation of pro-inflammatory genes and the upregulation of anti-inflammatory genes[4–6]. However, approximately 10% of patients with severe asthma exhibit steroid resistance[7], where exacerbations lead to bronchial epithelial cells releasing thymic stromal lymphopoietin (TSLP) in response to pathogenic stimuli[8]. Secreted TSLP primarily binds to its receptor complex (TSLPR/IL-7R) on dendritic cells (DCs), T helper 2 (T_H2) cells, type 2 innate lymphoid cells (ILC2), and alveolar macrophages (AMs), triggering downstream inflammatory responses via the phosphorylation of p38 MAPK (p-p38) and STAT3 (p-STAT3)[9–11]. p-p38 and p-STAT3 further induce the phosphorylation of the GR, modifying the conformational state of the unliganded GR, thereby impeding its binding to budesonide and subsequently preventing the nuclear translocation of the GR complex[12,13]. As a result of this cascade, there is an increase in immunoglobulin E (IgE) production, an elevated release of pro-inflammatory cytokines, and an enhanced recruitment of immune cells, ultimately compromising the therapeutic effectiveness of corticosteroids[4,12]. Although newly developed antibody-based therapeutics have tackled certain challenges associated with

[1]Shanghai Frontiers Science Center of Drug Target Identification and Delivery, School of Pharmaceutical Sciences, Shanghai Jiao Tong University, Shanghai, China. [2]National Key Laboratory of Innovative Immunotherapy, Shanghai Jiao Tong University, Shanghai, China. [3]Department of Chemical and Materials Engineering, New Jersey Institute of Technology, Newark, NJ, USA. [4]Department of Biomedical Engineering, New Jersey Institute of Technology, Newark, NJ, USA. ✉e-mail: xiaoyang.xu@njit.edu; xueqingzhang@sjtu.edu.cn

https://doi.org/10.1038/s41467-025-61114-4

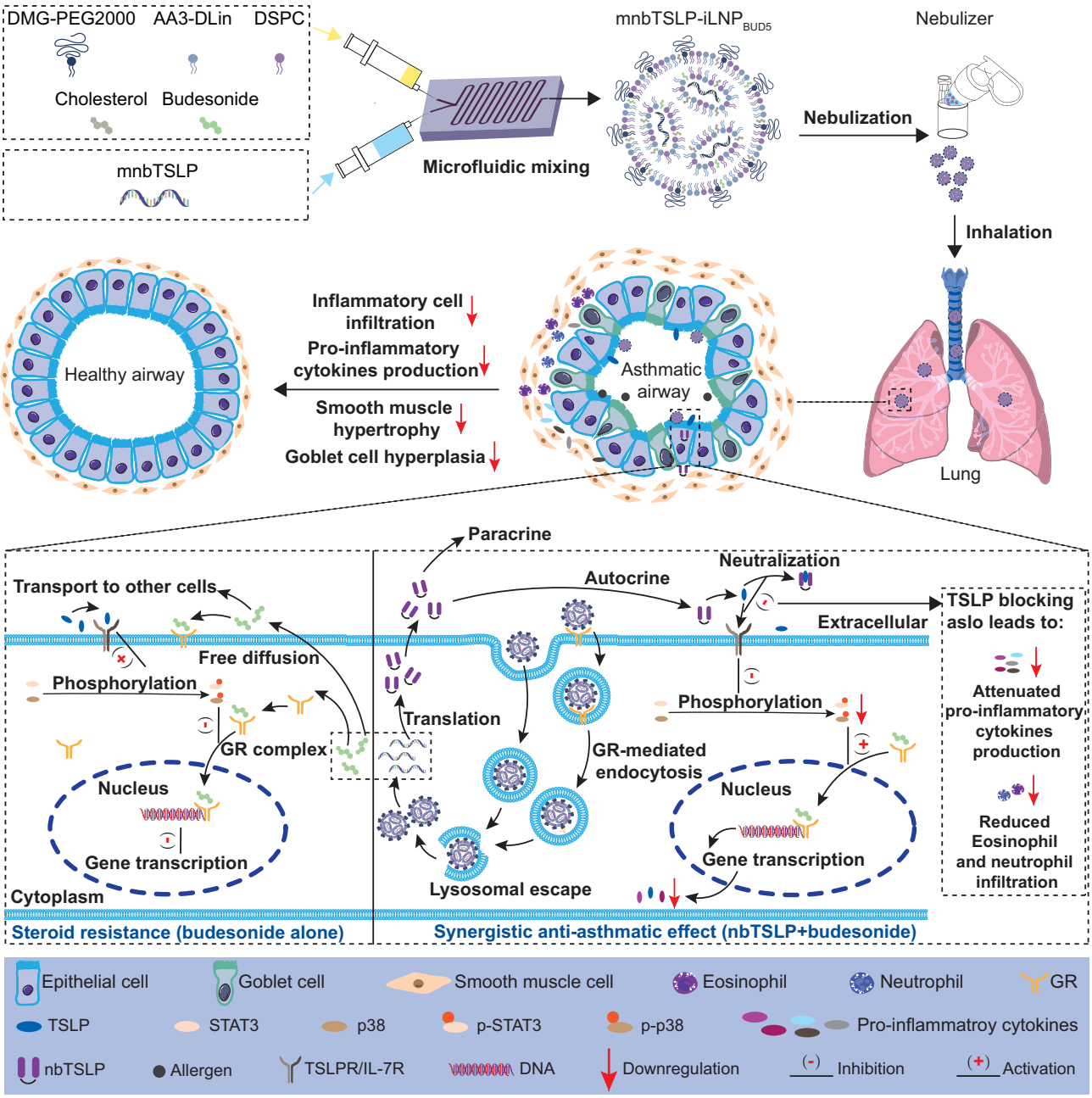

Fig. 1 | Schematic overview. mnbTSLP-iLNP$_{BUD5}$ self-assembles through microfluidics and is aerosolized with a vibrating mesh nebulizer for pulmonary delivery. After internalization via membrane fusion and GR-mediated endocytosis, mnbTSLP-iLNP$_{BUD5}$ escapes from lysosomes, releasing its cargo, mnbTSLP and budesonide, into the cytoplasm. The therapeutic mnbTSLP subsequently translates into nbTSLP, which is secreted extracellularly to neutralize overexpressed TSLP in the asthmatic airway environment, preventing the phosphorylation of STAT3 and p38 and restoring budesonide sensitivity. Consequently, the GR complex formed by budesonide's interaction with GR successfully translocates to the nucleus, modulating the transcription of inflammatory genes. Taken together, the synergistic combination of budesonide and nbTSLP alleviates asthma symptoms, including inflammatory cell infiltration, pro-inflammatory cytokine production, goblet cell hyperplasia, and smooth muscle hypertrophy, leading to the regression of asthma and the restoration of a healthy airway.

corticosteroid treatment in severe asthma through modulation of key cytokines (e.g., TSLP) and signaling pathways, their clinical application is constrained by off-target organ accumulation and the challenge of sustaining efficacious therapeutic lung concentrations when administered systemically[14,15]. There remains an unmet need for the development of effective targeted therapeutic strategies to treat severe asthma, particularly in instances of acquired steroid resistance.

Here, we present an inhalable combinatorial therapy, designated ASCEND (Alternative Steroids Co-delivering with mRNA Encoding Nanobodies), which integrates lipid nanoparticle (LNP)-mediated delivery of mRNA encoding a TSLP-blocking bivalent nanobody (mnbTSLP) with budesonide for the management of steroid-resistant asthma (Fig. 1). mRNA-based protein replacement therapy offers great promise due to its ability to express desired proteins or peptides

through tailored mRNA sequences[16,17]. In this regard, we have employed a nanoparticle-assisted inhalable mRNA therapeutic approach to achieve pulmonary delivery of anti-TSLP nanobody (nbTSLP), providing a non-invasive and highly patient-compliant treatment option. We hypothesize that the simultaneous pulmonary delivery of mnbTSLP and budesonide, encapsulated within a single inhalable nanocarrier, has the potential to rejuvenate budesonide sensitivity in corticosteroid-resistant asthma. mRNA-mediated expression of nbTSLP inhibits TSLP-induced phosphorylation of p38 and STAT3, thereby restoring the binding interaction between budesonide and GRs and promoting the nuclear translocation of the resultant GR complex. Consequently, the combination of mnbTSLP and budesonide may synergistically exert an anti-inflammatory effect through the inhibition of epithelial-derived TSLP-triggered T_H2 immune responses and the regulatory effects of budesonide on the transcriptional program of immune cells[9,18]. Given the heterogeneous nature of severe asthma, characterized by multiple underlying pathophysiological mechanisms[19,20], this combinatorial approach may help overcome the limitations of monotherapies that target a single cytokine or rely on a single anti-inflammatory mechanism.

Building upon our previously developed inhalable LNP (iLNP) platform[21], we have constructed an innovative formulation denoted as mnbTSLP-iLNP$_{BUD5}$, using budesonide as a partial alternative to cholesterol due to their structural similarities. We found that the integration of budesonide into the mnbTSLP-iLNP formulation, serving dual roles as a structural component for the LNP nanostructure and as a therapeutic agent, resulted in the mnbTSLP-iLNP$_{BUD5}$ demonstrating exceptional stability following nebulization, and markedly improved mnbTSLP-iLNP transfection efficiency in both in vitro and in vivo settings. This enhancement could be driven by the interaction of budesonide with its membrane receptor, alongside the internalization of LNPs via membrane fusion and endocytosis. In an OVA-induced acute asthma murine model, mnbTSLP-iLNP$_{BUD5}$ demonstrated superior efficacy in inhibiting airway remodeling and alleviating airway hyperresponsiveness compared to monotherapy with either budesonide or anti-TSLP antibody. This was evidenced by significant reductions in inflammation, mucus secretion, collagen deposition, and airway resistance. Interestingly, the budesonide content in mnbTSLP-iLNP$_{BUD5}$ is lower than that in the positive control group (Pulmicort), suggesting its potential to reduce the required budesonide dosage in asthma treatment. Administration of mnbTSLP-iLNP$_{BUD5}$ via inhalation notably reduced inflammatory cell infiltration, halted airway wall thickening, and restored airway resistance to normal levels in another OVA/TSLP-induced model of steroid-resistant asthma, where budesonide monotherapy alone proved ineffective. The synergistic effect of mnbTSLP and budesonide stems from mnbTSLP's ability to target the upstream root causes of airway inflammation, while budesonide restores its efficacy in regulating downstream inflammatory gene transcription. This interplay is primarily driven by mnbTSLP's modulation of the p38 MAPK and STAT3 signaling pathways. In this study, we first demonstrated the utilization of iLNPs incorporating mRNA to block TSLP signaling and budesonide to regulate the inflammatory cytokine expression profile in two preclinical asthma models, highlighting the synergistic effect of the ASCEND approach for repairing injured airway epithelium. Overall, the ASCEND platform offers a versatile solution for the concurrent inhalation delivery of mRNA therapeutics and steroids, exhibiting potent therapeutic potential in the management of asthma and various other respiratory conditions.

Results

Optimization of budesonide-containing iLNP formulations for nebulized delivery

Developing aerosol-based nucleic acid carriers that are resistant to damage induced by nebulization is essential for the effective pulmonary delivery of nucleic acid therapeutics[22]. Utilizing our previously developed ionizable lipid AA3-DLin, along with the incorporation of poloxamer 188 as an excipient to enhance nebulization efficiency[21], we formulated budesonide-containing iLNPs for aerosol delivery of mRNA. Through microfluidic mixing, five iLNPs were prepared by substituting cholesterol with varying molar percentages (0%, 5%, 9.5%, 14%, and 19%) of budesonide (Fig. 2a). We examined the impact of budesonide substitution on the physicochemical properties of the iLNPs, both before and after nebulization. Figure 2b–d illustrate the changes in size, zeta potential, and polydispersity index (PDI) of iLNPs before and after nebulization, as determined by dynamic light scattering (DLS). The results indicate that introducing 5% budesonide caused minimal changes in nanoparticle size, PDI, and zeta potential compared to the other four formulations after nebulization. Specifically, mRNA-iLNP$_{BUD5}$ showed almost no change in PDI, zeta potential, and size (<1.2-fold change), similar to those observed for mRNA-iLNP$_{BUD0}$, confirming its ability to maintain the colloidal stability of the LNPs during the nebulization process. Figure 2e demonstrates that with an increasing incorporation of budesonide, the encapsulation efficiency (EE) of the LNPs decreased from approximately 90% to 49%, as measured by the Ribogreen assay. Upon nebulization, mRNA-iLNP$_{BUD5}$ showed a 2% decline in EE, reflecting a trend similar to that of mRNA-iLNP$_{BUD0}$ (3%). In contrast, the two formulations containing 14% or 19% budesonide experienced a significant 20% loss in EE, while mRNA-iLNP$_{BUD9.5}$ had a 10% reduction in mRNA encapsulation after nebulization. These results suggest that high concentrations of budesonide are associated with instability and mRNA leakage from the iLNPs during the nebulization process.

We then incubated the bronchial epithelial cell line BEAS-2B with the specified LNP aerosols, generated by nebulization and loaded with mRNA encoding EGFP (mEGFP), to assess transfection efficiency. Using fluorescence microscopy, we observed that mEGFP-iLNP$_{BUD5}$ exhibited the most intense green fluorescence signal among the five indicated iLNPs (Supplementary Fig. 1). Flow cytometry analysis further corroborated this observation, revealing a significant increase in EGFP expression in cells transfected with mEGFP-iLNP$_{BUD5}$, with approximately 72% of cells exhibiting EGFP positivity (Supplementary Fig. 2 and Fig. 2f). To elucidate the role of budesonide in enhancing the transfection efficiency of mEGFP-iLNP$_{BUD5}$, we pre-treated BEAS-2B cells with the GR antagonist mifepristone before adding nebulized iLNPs, then measured transfection efficiency by flow cytometry[23–25]. As shown in Fig. 2g and Supplementary Fig. 3, the mEGFP-iLNP$_{BUD0}$-mediated transfection was unaffected by mifepristone, with the percentage of EGFP-positive cells consistently remaining at 55%. Conversely, mifepristone markedly reduced the transfection efficiency of mEGFP-iLNP$_{BUD5}$, with the EGFP-positive cell population decreasing from approximately 76% to around 58%. This observation supports the hypothesis that the enhanced EGFP expression in mEGFP-iLNP$_{BUD5}$ is mediated by GR-dependent endocytosis. However, as the concentration of budesonide incorporated into the iLNPs increased, transfection efficiency decreased substantially, with the EGFP-positive cell population dropping from ~39% in nebulized mEGFP-iLNP$_{BUD9.5}$ to ~6% in nebulized mEGFP-iLNP$_{BUD19}$ (Fig. 2f). This reduction is likely attributed to poorer structural stability and a lower EE, both of which adversely affect transfection efficiency.

To evaluate the in vivo transfection efficacy mediated by iLNPs, BALB/c mice were nebulized with luciferase mRNA-loaded iLNPs (mLuc-iLNP$_{BUD0}$, mLuc-iLNP$_{BUD5}$, mLuc-iLNP$_{BUD9.5}$, mLuc-iLNP$_{BUD14}$, and mLuc-iLNP$_{BUD19}$) using a vibrating mesh nebulizer, and primary organs were harvested and analyzed with the IVIS imaging system six hours after a single-dose inhalation. Quantification analysis of the bioluminescence signals indicated that luciferase activity was confined to the lungs (Lu), with no detectable bioluminescence signals in other organs, including heart (He), liver (Li), spleen (Sp), and kidneys (Ki) (Fig. 2h, i). mLuc-iLNP$_{BUD5}$ induced more efficient luciferase expression in the lungs compared to the other iLNP formulations, consistent with

https://doi.org/10.1038/s41467-025-61114-4

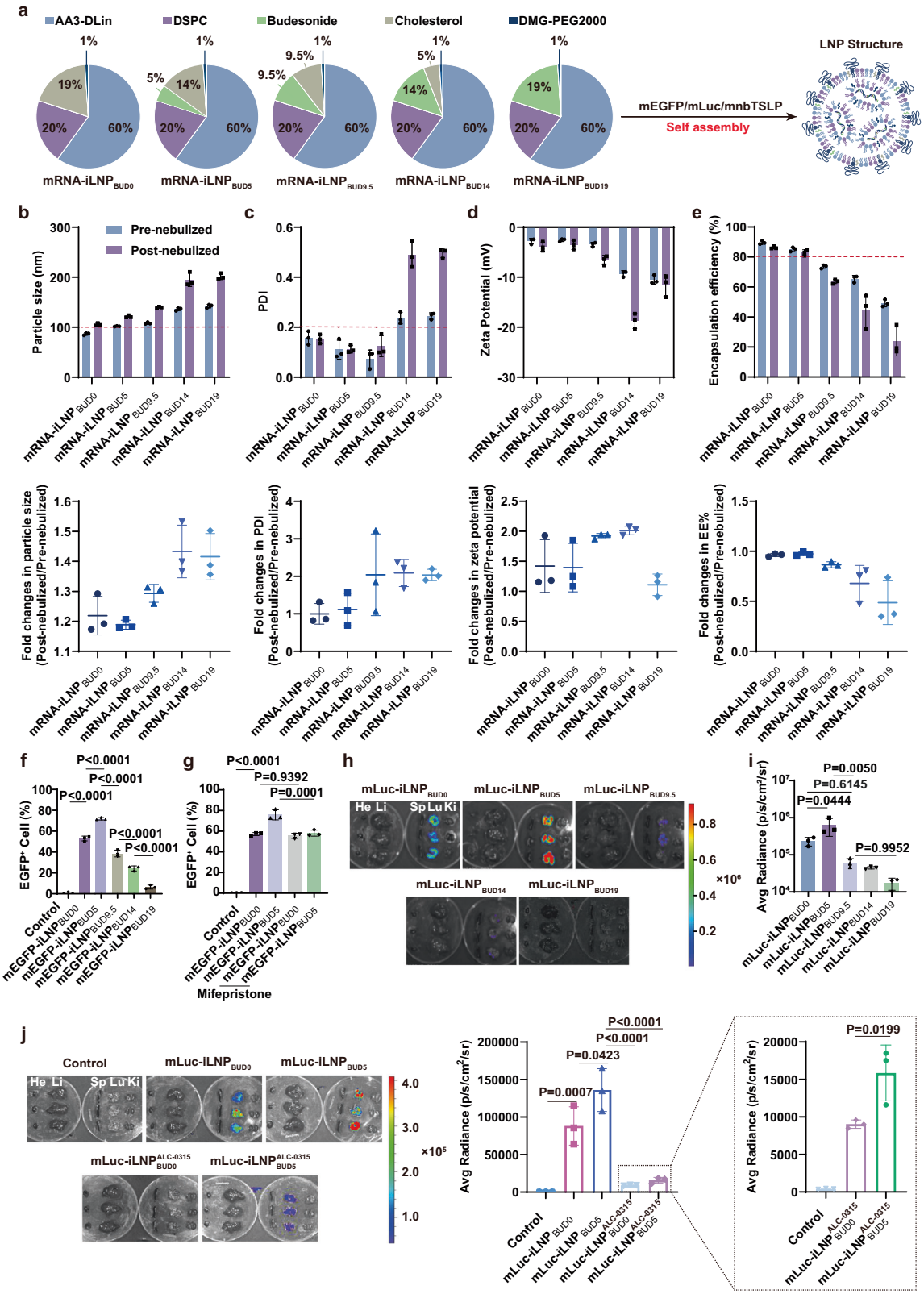

the cellular transfection data. We also selected two ALC-0315-based formulations as controls for in vivo luciferase expression evaluations: (1) a clinically approved formulation used in Pfizer's COVID-19 mRNA vaccine (mLuc-iLNP$^{ALC\text{-}0315}_{BUD0}$) containing 46.3 mol% ALC-0315, 9.4 mol% DSPC, 42.7 mol% cholesterol, and 1.6 mol% DMG-PEG2000; and (2) an optimized formulation from our screening study (mLuc-iLNP$^{ALC\text{-}0315}_{BUD5}$) composed of 60 mol% ALC-0315, 20 mol% DSPC, 14 mol% cholesterol, 5 mol% budesonide, and 1 mol% DMG-PEG2000. Compared to the ALC-0315 controls, the AA3-DLin formulations (mLuc-iLNP$_{BUD0}$ and mLuc-iLNP$_{BUD5}$) exhibited significantly stronger luminescent signals in the lungs (Fig. 2j), consistent with our previous finding that AA3-DLin LNPs surpass ALC-0315 LNPs in mRNA delivery efficacy[26]. Interestingly, even within the ALC-0315 group, the iLNP containing 5 mol% budesonide demonstrated higher luciferase

Fig. 2 | Preparation and screening of mRNA-iLNPs for aerosolized delivery. **a** Schematic diagram of iLNP formulations incorporating the indicated molar ratios of budesonide (0%, 5%, 9.5%, 14%, and 19%). **b**–**e**, Particle size (**b**), PDI (**c**), zeta potential (**d**), EE (**e**) and the corresponding fold changes of the various mRNA-iLNPs before and after nebulization. **f** Percentage of EGFP-positive BEAS-2B cells after a 6-h incubation with the designated mEGFP-iLNPs, as determined by flow cytometry. **g** Mifepristone reduces the proportion of EGFP-positive BEAS-2B cells after a 6-h transfection with mEGFP-iLNP$_{BUD5}$, yet has no effect on cells transfected with mEGFP-iLNP$_{BUD0}$. Untreated BEAS-2B cells served as control (**f, g**). **h** In vivo bioluminescence images of major organs collected from BALB/c mice, 6 h after inhalation of the indicated mLuc-iLNPs. He, Li, Sp, Lu, and Ki represent the heart, liver, spleen, lung, and kidneys, respectively. **i** Quantification analysis of luciferase signals in mouse lungs using Living Image 4.5 software. **j** IVIS imaging and quantitative analysis of luminescence signals from the major organs of mice nebulized with AA3-DLin or ALC-0315 containing mLuc-iLNPs. He, Li, Sp, Lu, and Ki represent the heart, liver, spleen, lung, and kidneys, respectively. Results are presented as mean ± s.d, $n = 3$ biologically independent mice or samples per group (**b**–**j**). Significant differences were assessed using a one-way ANOVA with Tukey's multiple comparisons test (**f, g, i, j**). *P* values as indicated. Source data are provided as a Source Data file.

expression than the iLNP without budesonide (1.8-fold difference), indicating that the ASCEND approach can also enhance the performance of commercial ALC-0315 LNPs. Most strikingly, the ASCEND-optimized AA3-DLin formulation achieved the highest efficacy, with luminescence intensities 1.6-fold, 15.2-fold, and 9.0-fold higher than mLuc-iLNP$_{BUD0}$, mLuc-iLNP$^{ALC\text{-}0315}_{BUD0}$, and mLuc-iLNP$^{ALC\text{-}0315}_{BUD5}$, respectively. These results demonstrate that mRNA-iLNP$_{BUD5}$ possesses optimal physicochemical properties and efficiently facilitates lung-targeted mRNA expression following nebulization. Taken together, we selected mRNA-iLNP$_{BUD5}$ for the following experiments.

Characterization of mRNA-iLNP$_{BUD5}$ for efficient aerosol-based delivery

Cryogenic transmission electron microscopy (Cryo-TEM) was employed to analyze the morphology, size, and spatial distribution of mEGFP-iLNP$_{BUD5}$. As shown in the Cryo-TEM images, mEGFP-iLNP$_{BUD5}$ exhibited a spherical morphology with a uniform size distribution and even particle dispersion across the observed field, both before and after nebulization (Fig. 3a). Consistent with the Cryo-TEM findings, DLS data also revealed that the nebulization process did not cause any changes in the average particle size or nanostructure of mEGFP-iLNP$_{BUD5}$ (Fig. 3b). DLS data measured at the predetermined time points showed a steady trend, with the particle size remaining around 100 nm throughout the test period, suggesting that mEGFP-iLNP$_{BUD5}$ retains its colloidal stability for at least 30 days under 4 °C storage conditions (Fig. 3c). Additionally, we monitored the hydrodynamic size of the iLNP formulation in PBS containing 10% fetal bovine serum (FBS) at 37 °C, at both pH 7.4 (representing normal physiological conditions) and pH 6.8 (mimicking the mildly acidic environment of asthmatic pulmonary tissues). After 24 h of incubation, DLS measurements revealed no significant change in particle size, demonstrating that mEGFP-iLNP$_{BUD5}$ retains stable in both neutral and mildly acidic physiological conditions (Fig. 3d).

To further assess the stability of iLNP$_{BUD5}$ under various stress conditions, we conducted an additional study comparing refrigerated (4 °C) and frozen (−20 °C, with or without cryoprotectant) storage, specifically focusing on the formulation's resistance to nebulization-induced damage. As shown in Supplementary Fig. 4a and 4b, mRNA-iLNP$_{BUD5}$ stored at 4 °C for 7 days maintained physical stability after nebulization, showing minimal variations in particle size (< 1.2-fold) and PDI (< 1.3-fold). However, extended 30-day storage at 4 °C led to post-nebulization instability, with particle size and PDI increasing by 1.3-fold and 1.6-fold, respectively. Notably, cryoprotectant-free samples frozen at −20 °C for 30 days exhibited severe instability with significant increases in particle size and PDI both before and after nebulization, whereas formulations containing 5% sucrose retained stability comparable to fresh preparations. Beyond physicochemical characterization, we systematically assessed both in vitro and in vivo biological functionality. Flow cytometry analysis (Supplementary Fig. 4c) showed that approximately 86% of cells were EGFP-positive following transfection with mEGFP-iLNP$_{BUD5}$ stored at 4 °C for 7 days, which then declined moderately to 63% after 30 days. This reduction of in vitro transfection efficiency might be correlated with mRNA degradation under prolonged suboptimal storage[27]. The cryoprotectant-free frozen mRNA-iLNP$_{BUD5}$ samples showed drastic functional impairment, with transfection efficiency dropping from ~84% to ~33%. In contrast, 5% sucrose effectively stabilized the LNP structure during 30-day storage at −20 °C, as evidenced by mEGFP-iLNP$_{BUD5}$ containing the cryoprotectant inducing approximately 84% EGFP-positive cells. This cryoprotective effect was further validated in vivo, where mLuc-iLNP$_{BUD5}$ maintained pulmonary luciferase expression profiles that were consistent with their in vitro transfection efficiency across different storage conditions (Supplementary Fig. 4d and 4e). Collectively, these results demonstrate that optimized cryopreservation strategies, particularly the incorporation of sucrose as a stabilizer, enable iLNPs to retain both structural integrity and functional transfection capacity during long-term storage.

The mucus layer acts as a lung-specific barrier, limiting the transfection of iLNP-based nebulized mRNA into the bronchial epithelium[28]. To investigate this, we evaluated the mucus penetration behavior of mRNA-iLNP$_{BUD5}$ using an artificial model with a mucus upper layer and a gelatin lower layer (Fig. 3e). Naked Cy5-labeled mRNA (mRNA^{Cy5}) and iLNP$_{BUD5}$ encapsulating Cy5-labeled mRNA (mRNA^{Cy5}-iLNP$_{BUD5}$) were introduced into the upper layer of the artificial mucus model, and fluorescence intensity of the gelatin layer was measured at 0.5, 2, and 4 h. The mRNA^{Cy5}-iLNP$_{BUD5}$ treatment displayed significantly higher fluorescence than the naked mRNA^{Cy5} treatment at each time point, with a notable increase in iLNP penetration observed as the incubation period was extended (Fig 3f). These findings indicate that mRNA^{Cy5}-iLNP$_{BUD5}$ facilitates efficient transmucosal delivery of mRNA^{Cy5}.

We then incubated Lysotracker Green-labeled 16HBE cells with mRNA^{Cy5}-iLNP$_{BUD5}$ to study the mRNA escape process from lysosomes. Figure 3g shows the co-localization of red fluorescence signals from mRNA^{Cy5} and green fluorescence signals from the lysosomes at 0.5 h. This co-localization increased at 2 h, as indicated by the bright orange fluorescence resulting from the extensive overlap of the red and green signals. By 4 h, the signals were completely separated, suggesting the release of mRNA^{Cy5} from the lysosomes into the cytoplasm for protein translation. The Pearson's colocalization values were consistent with the immunofluorescence staining results (Supplementary Fig. 5).

The mEGFP-iLNP$_{BUD5}$ aerosol was collected post-nebulization and incubated with 16HBE cells. Laser scanning confocal microscopy (LSCM) images showed strong and uniform green fluorescence surrounding the blue nuclear signal, indicating efficient mRNA delivery and expression mediated by the aerosolized iLNP (Fig. 3h). Supplementary Fig. 6a unveiled that the aerosolized mEGFP-iLNP$_{BUD5}$ mediated transfection in a dose-dependent manner, with the highest EGFP fluorescence observed at 4 μg. As shown by the live/dead cell staining assay results, no cytotoxicity was observed in 16HBE cells incubated with mEGFP-iLNP$_{BUD5}$ at mRNA concentrations up to 4 μg and transfection durations of up to 5 days (Supplementary Fig. 6b). The above results demonstrate that mRNA-iLNP$_{BUD5}$ exhibits good stability, tolerance to nebulization-induced damage, excellent transmucosal penetration, high transfection efficiency, and favorable safety, making it a promising vector for inhalable mRNA therapy.

https://doi.org/10.1038/s41467-025-61114-4

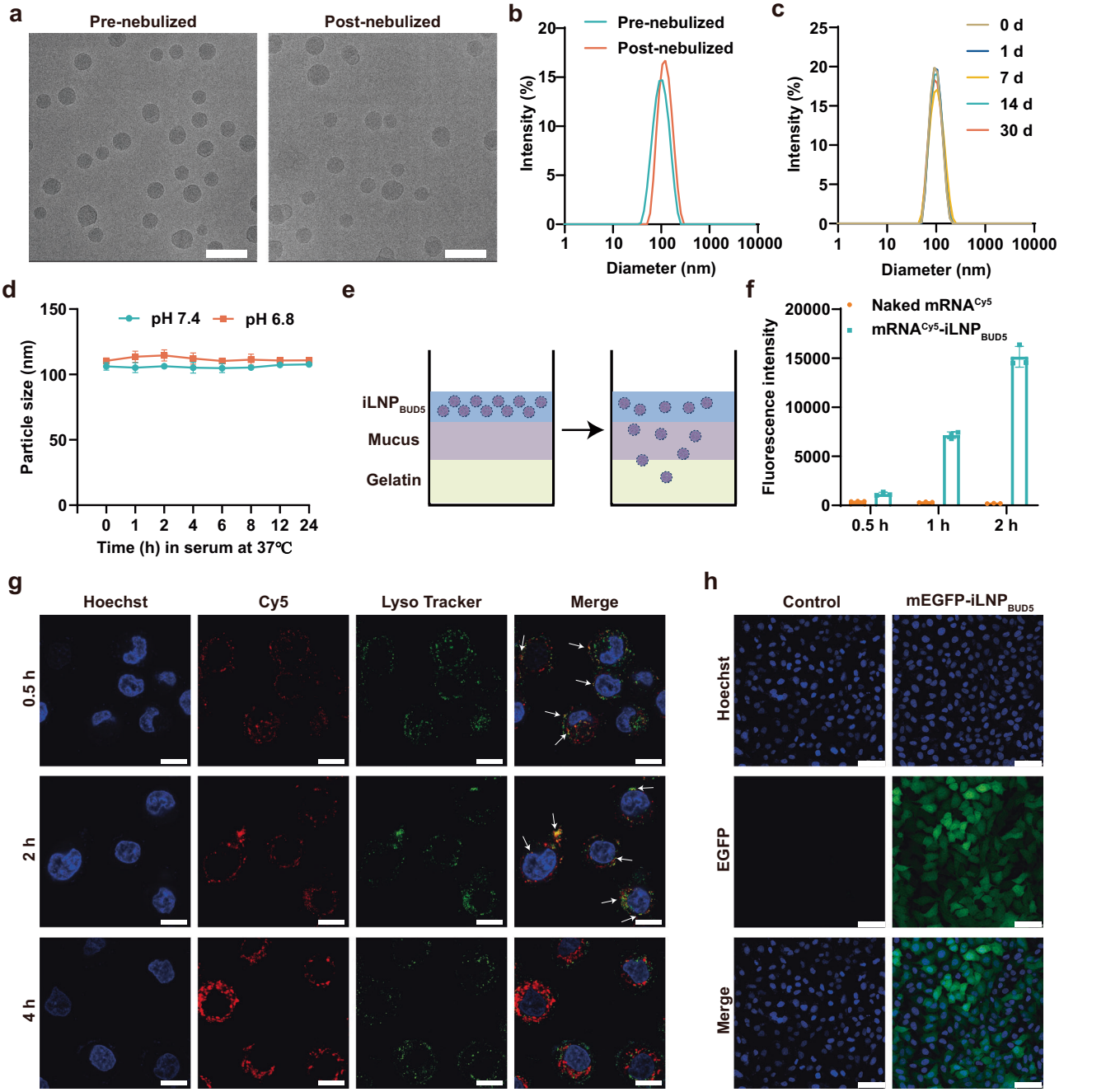

Fig. 3 | Characterization of mRNA-iLNP$_{BUD5}$ for aerosol-based delivery. a, b Representative Cryo-TEM images (**a**) and size distribution (**b**) of mEGFP-iLNP$_{BUD5}$ before and after nebulization. Scale bars, 100 nm. **c** Size distribution of mEGFP-iLNP$_{BUD5}$ at different time points during 30 days of storage at 4 °C. **d** The particle size of mEGFP-iLNP$_{BUD5}$ was evaluated at predetermined time intervals during incubation in PBS supplemented with 10% FBS, at pH values of 7.4 or 6.8, and at a temperature of 37 °C. **e** Illustrative schematic depicting the penetration of iLNP$_{BUD5}$ through an in vitro mucus model. **f** Fluorescence intensity profiles of the gelatin layer at different time points following the addition of mRNA^{Cy5}-iLNP$_{BUD5}$ and naked mRNA^{Cy5} into the artificial mucus model. **g** Representative LSCM images of 16HBE cells at 0.5, 2, and 4 h after incubation with iLNP$_{BUD5}$ encapsulating mRNA^{Cy5}. Blue fluorescence indicates nucleus, red fluorescence indicates mRNA^{Cy5}, and green fluorescence indicates lysosomes. White arrows indicate the colocalization of lysosomes with mRNA^{Cy5}. Scale bars, 20 μm. **h** Representative LSCM images demonstrating EGFP expression in 16HBE cells after 24 h of incubation with mEGFP-iLNP$_{BUD5}$. Blue and green fluorescence indicates nucleus and EGFP, respectively. Scale bars, 50 μm. Results are presented as mean ± s.d, $n = 3$ biologically independent samples per group (**d, f**). Source data are provided as a Source Data file.

Design and in vitro validation of mnbTSLP

The nucleic acid and amino acid sequence of nbTSLP was shown in Supplementary Tables 1 and 2. Figure 4a shows the complete sequence of mnbTSLP, which includes a 5′ cap, a 5′ untranslated region (5′ UTR), the initiation codon, the open reading frame (ORF), a 3′ untranslated region (3′ UTR), and a 3′ poly(A) tail. The ORF encodes secretory peptides, the heavy chain variable region (VHH) of the antibody, binding peptides, a detection tag (Flag-Tag), and a purification tag (His-Tag), forming the essential portion of the mRNA that is translated into nbTSLP.

We encapsulated mnbTSLP into iLNP$_{BUD5}$ and studied the protective effect of iLNP$_{BUD5}$ on mnbTSLP by incubating naked mnbTSLP and mnbTSLP-iLNP$_{BUD5}$ with 10% FBS for various time intervals, respectively. Agarose gel electrophoresis analysis displayed in Fig. 4b

https://doi.org/10.1038/s41467-025-61114-4

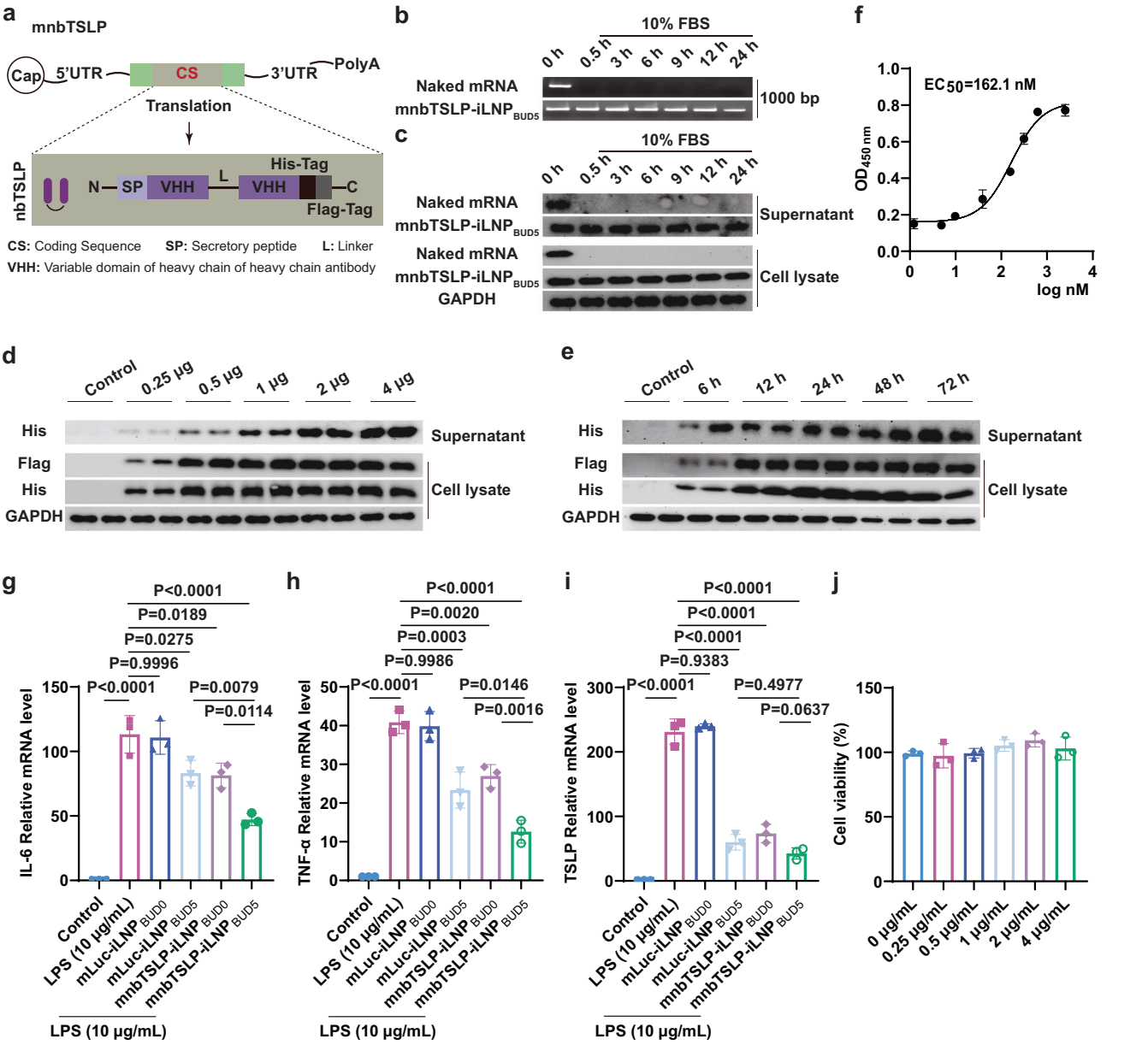

Fig. 4 | Design and in vitro validation of mnbTSLP-iLNP$_{BUD5}$. **a** Design of mnbTSLP sequence. **b** Stability assessment of naked mnbTSLP and iLNP$_{BUD5}$-encapsulated mnbTSLP in the presence of 10% FBS by agarose gel electrophoresis. **c** Western blot analysis examining the effect of 10% FBS on the transfection efficiency of mnbTSLP mediated by iLNP$_{BUD5}$ revealed a protein band at 35 kDa. Flag-Tag was used for detection. GAPDH was used as a housekeeping standard. **d, e** Western blot analysis of dose- (**d**) and time-dependent (**e**) expression of mnbTSLP mediated by iLNP$_{BUD5}$. His- and Flag-Tags were used for detection. GAPDH was used as a housekeeping standard. **f** Binding affinity between TSLP and nbTSLP was detected by ELISA assays. **g-i**, qRT-PCR analysis of IL-6 (**g**), TNF-α (**h**), and TSLP (i) mRNA levels in 16HBE cells stimulated with 10 μg/mL LPS for 4 h, followed by a 24-h incubation with the indicated iLNPs. Untreated 16HBE cells were used as control. (**j**) The viability of 16HBE cells was assessed using the CCK-8 assay after a 24-h incubation with increasing concentrations of mnbTSLP-iLNP$_{BUD5}$. Results are presented as mean ± s.d, $n = 2$ (**f**) and $n = 3$ (**g-j**) biologically independent samples. Significant differences were assessed using a one-way ANOVA with Tukey's multiple comparisons test (**g-i**). P values as indicated. Source data are provided as a Source Data file.

demonstrated that the naked mnbTSLP degraded rapidly, with no detectable band at 0.5 h. In contrast, the mRNA extracted from mnbTSLP-iLNP$_{BUD5}$ exhibited a single, intense band at 1000 bp, indicating that it maintained structural integrity when exposed to 10% FBS for up to 24 h. The naked mnbTSLP or mnbTSLP-iLNP$_{BUD5}$, treated with 10% FBS for the specified duration, was then separately incubated with 16HBE cells to evaluate mRNA-mediated transfection efficiency. Figure 4c shows that mnbTSLP encapsulated in iLNP$_{BUD5}$ retained its capacity to translate into nbTSLP in the presence of serum, as evidenced by an intense protein band around 35 kDa at all time points examined. In contrast, when lipofectamine 3000 transfection reagent (Lipo 3000) was used as the carrier, the naked mnbTSLP lost its ability to mediate protein translation in 16HBE cells as early as 0.5 h after serum exposure. The results indicate that mnbTSLP-iLNP$_{BUD5}$ effectively protects the internal mnbTSLP from structural and functional alterations caused by the extracellular environment.

Western blot analysis showed that iLNP$_{BUD5}$ mediated nbTSLP expression and secretion in both cell culture supernatants and cell lysates in a dose- and time-dependent pattern. Figure 4d and Supplementary Fig. 7a demonstrate efficient nbTSLP translation in supernatants and cell lysates, particularly with high mRNA doses of 2 μg and 4 μg. Expression in the cell lysates peaked at 48 h, while supernatant

levels continued to rise over 72 h, possibly resulting from a lag in secretion (Fig. 4e and Supplementary Fig. 7b). These findings suggest that mnbTSLP-iLNP$_{BUD5}$ effectively mediates nbTSLP production and secretion in a sustained manner for at least 3 days, maintaining consistently high levels of nbTSLP, and providing valuable insight for determining the optimal administration interval in therapeutic experiments.

mnbTSLP-iLNP$_{BUD5}$ exerts a potent anti-inflammatory effect in vitro

nbTSLP was harvested from the cell culture supernatants after transfecting HEK293T cells with mnbTSLP for three days, followed by purification using nickel affinity chromatography. The production of nbTSLP was confirmed using Coomassie Brilliant Blue staining and Western blot analysis, as indicated by a single 35 kDa protein band (Supplementary Fig. 8a,b). The binding affinity of the purified nbTSLP to TSLP was examined by enzyme-linked immunosorbent assay (ELISA), yielding an EC50 value of approximately 162.1 nM (Fig. 4f).

We then established a lipopolysaccharide (LPS)-induced inflammatory 16HBE cell model to evaluate the in vitro anti-inflammation effects of mnbTSLP-iLNP$_{BUD5}$ (Supplementary Fig. 9). qRT-PCR analysis revealed that LPS treatment promoted the mRNA levels of IL-6, TNF-α, and TSLP in 16HBE cells, and mnbTSLP-iLNP$_{BUD5}$ significantly suppressed the mRNA expression of IL-6 and TNF-α, outperforming both budesonide monotherapy (mLuc-iLNP$_{BUD5}$) and nbTSLP alone (mnbTSLP-iLNP$_{BUD0}$) (Fig. 4g–i). Figure 4i shows a significant reduction in TSLP mRNA levels in cells treated with mnbTSLP-iLNP$_{BUD0}$ and mnbTSLP-iLNP$_{BUD5}$, suggesting the presence of a positive feedback mechanism in TSLP induction during the LPS-induced inflammatory response. This is likely due to TSLP's downstream effector cells not only responding to TSLP via TSLPR/IL-7R but also serving as a key source of TSLP[29,30]. Notably, mLuc-iLNP$_{BUD5}$ also significantly reduced TSLP mRNA expression, likely due to budesonide's ability to regulate the transcription of pro-inflammatory cytokines, including TSLP, and suppress their production[30]. As shown in the cell counting kit-8 (CCK8) assay, mnbTSLP-iLNP$_{BUD5}$ did not affect the proliferation of 16HBE cells within the tested concentration range, including at the highest concentration of 4 μg/mL, indicating its non-toxic nature (Fig. 4j). As assessed, mnbTSLP-iLNP$_{BUD5}$ demonstrated excellent mRNA stability, high affinity binding to TSLP, a favorable safety profile in 16HBE cells, and exceptional anti-inflammatory effects, providing preliminary support for its potential use in treating asthmatic mice in subsequent studies.

Inhaled mnbTSLP-iLNP$_{BUD5}$ reverses OVA-induced pulmonary airway remodeling and alleviates AHR in a mouse model of severe asthma

mnbTSLP-iLNP$^{Cy5}_{BUD5}$, prepared using Cy5-labeled cholesterol, was administered to BALB/c mice via a vibrating mesh nebulizer to evaluate its in vivo biodistribution and pulmonary deposition. IVIS images of organs harvested from mice treated with the indicated groups showed that the majority of fluorescent signals from mnbTSLP-iLNP$^{Cy5}_{BUD5}$ were concentrated in the lungs, with minimal signal detected in the heart, liver, spleen, and kidneys, confirming the successful pulmonary delivery of nebulized mnbTSLP-iLNP$^{Cy5}_{BUD5}$ (Supplementary Fig. 10a). The confocal microscopic images depicted a homogeneous distribution of mnbTSLP-iLNP$^{Cy5}_{BUD5}$ throughout the whole lung, with intense red fluorescence surrounding the bronchi and alveoli (Supplementary Fig. 10b).

As illustrated in Supplementary Fig. 11a, we established an acute severe asthma model in which mice were sensitized with weekly intraperitoneal OVA/Aluminum Hydroxide Gels Adjuvant (Alum) injections for 2 weeks (days 1 to 14), followed by daily intranasal OVA challenges for an additional week (days 21 to 27), and then sacrificed for analysis 48 h after the final challenge. Compared to the healthy group, mice receiving an OVA challenge dose of 20 μg showed minimal inflammatory cell recruitment in the airways, whereas a 50 μg OVA challenge induced significant inflammation, confirming the successful establishment of a severe asthma model (Supplementary Fig. 11b). Based on these observations, we selected the high-dose (50 μg) OVA-induced asthma model for the subsequent experiment.

To delineate the pulmonary cell targeting profile of nebulized iLNP$_{BUD5}$, we administered mnbTSLP-iLNP$^{Cy5}_{BUD5}$ to OVA-induced asthmatic mice using nose-only exposure chambers. Lung tissues were harvested 6 h post-administration, enzymatically dissociated, and immunostained with lineage-specific markers: CD31+ for endothelial cells, CD45+ for immune cells, and EpCAM+ for epithelial cells. The Cy5 fluorescence in these lung cell populations was subsequently analyzed by flow cytometry. Supplementary Fig. 12 revealed that the nebulized iLNP$^{Cy5}_{BUD5}$ exhibited differential cellular uptake: the strongest Cy5 signal was detected in immune cells (~ 43.3%), followed by epithelial cells (~ 8.43%), with minimal detection in endothelial cells (~ 1.13%). These results suggest that immune and epithelial cells play a primary role in the lung distribution and protein expression of nebulized iLNP$_{BUD5}$, which is consistent with previously reported distribution patterns of inhaled LNPs[31]. The preferential uptake by CD45+ immune cells may be mechanistically explained by asthma-induced pulmonary inflammation. Clinical and preclinical evidence confirms that allergic airway remodeling increases CD45+ leukocyte infiltration, creating a cellular microenvironment that enhances LNP phagocytosis[32,33]. Concurrently, the observed epithelial uptake (~ 8.43%) likely reflects basal nanoparticle deposition on airway surfaces, consistent with bronchial epithelial cells constituting 10–15% of total lung cellularity in murine models[34].

In the in vivo pharmacodynamic evaluation experiment, the mice were randomly divided into the indicated groups and administered therapeutic agents (mLuc-iLNP$_{BUD0}$, Pulmicort, mLuc-iLNP$_{BUD5}$, mnbTSLP-iLNP$_{BUD0}$, and mnbTSLP-iLNP$_{BUD5}$) via inhalation on days 21, 24, and 27. Prior to administration, mRNA concentration was measured using the RiboGreen assay, while budesonide concentration was determined by High-Performance Liquid Chromatography (HPLC). The single inhalation dose of mRNA (mLuc and mnbTSLP) was set at 30 μg per mouse, with the corresponding budesonide dose calculated to be approximately 24 μg (Supplementary Fig. 13).

Histological images showed reduced lung inflammation, airway wall thickening, mucus production, and collagen fiber accumulation in the airways of mice treated with inhaled Pulmicort, mLuc-iLNP$_{BUD5}$, or mnbTSLP-iLNP$_{BUD0}$. Notably, mice treated with inhaled mnbTSLP-iLNP$_{BUD5}$ exhibited lung morphology nearly identical to control levels, as evidenced by minimal changes in airway wall thickness, reduced inflammatory cell infiltration, mucus secretion, and collagen deposition typically associated with asthmatic progression (Fig. 5b). As shown in Fig. 5c–f, treatment with inhaled mnbTSLP-iLNP$_{BUD5}$ reduced airway thickness from 182 μm to 66 μm, inflammatory cell percentage from 36% to 5%, mucus production from 13% to 3%, and collagen content from 14% to 3%, reaching levels similar to those in the healthy group. Quantification analysis of H&E, PAS, and Masson stains using ImageJ software further confirmed that inhaled mnbTSLP-iLNP$_{BUD5}$ restored pulmonary airway homeostasis in mice, surpassing the efficacy of all monotherapy treatments.

We also collected bronchoalveolar lavage fluid (BALF) and serum samples at the end of the experiment to assess immunological biomarkers associated with asthma responses, including the quantification analysis of inflammatory cytokines, immune cells, and IgE. Western blot analysis detecting Flag-tag in BALF protein extracted from mice treated with mnbTSLP-iLNP$_{BUD5}$ showed intense bands at around 35 kDa, indicating successful secretion of nbTSLP (Supplementary Fig. 14). Treatment with inhaled mnbTSLP-iLNP$_{BUD5}$ resulted in a significant reduction in eosinophil and neutrophil counts in the BALF, as assessed using a Diff-Quik Stain kit. In contrast, only modest

https://doi.org/10.1038/s41467-025-61114-4

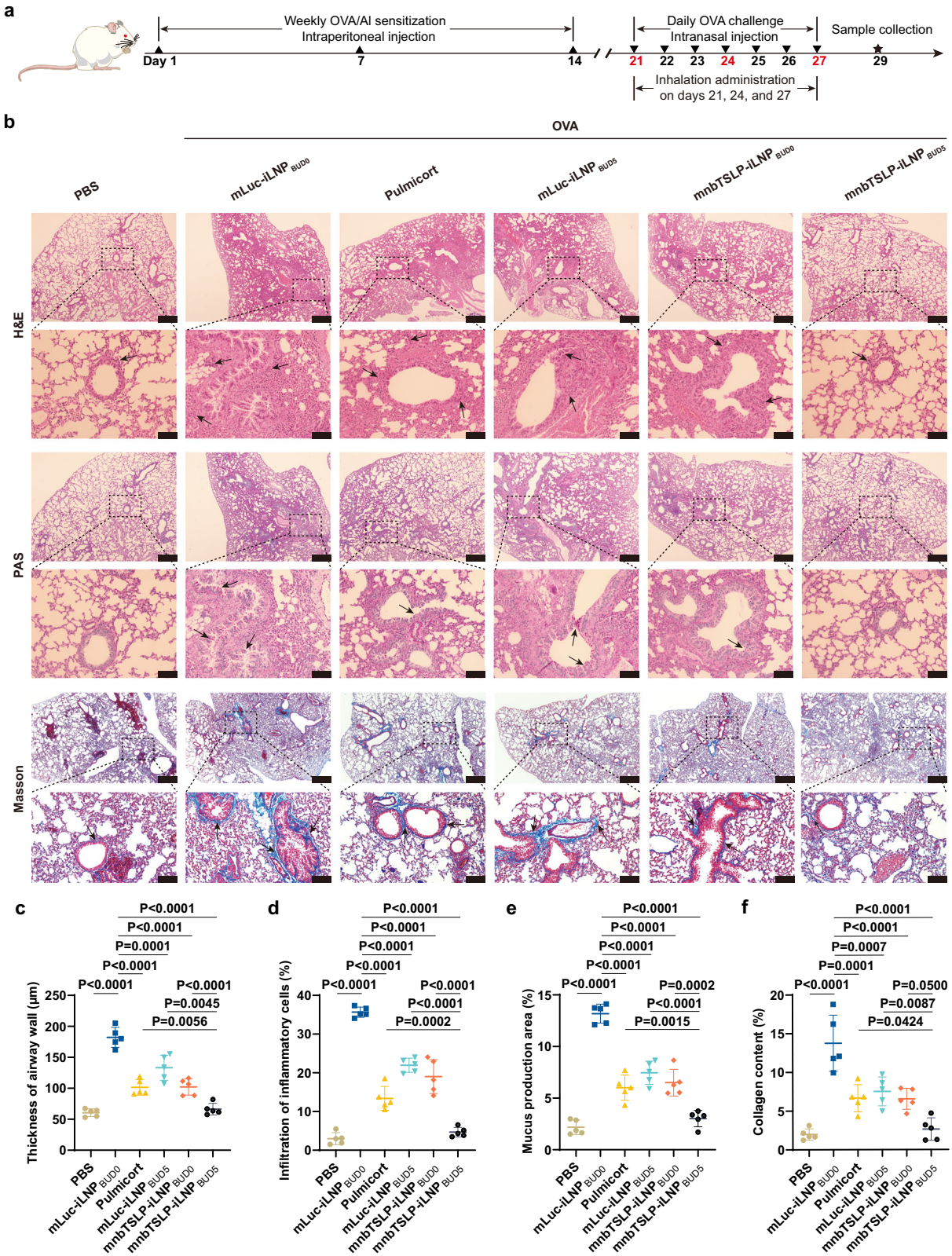

Fig. 5 | Inhalation of mnbTSLP-iLNP$_{BUD5}$ mitigates airway damage in established acute asthma models. a Schematic illustration of the OVA-induced asthma model and treatment regimen in BALB/c mice. **b** Histological analysis of lung sections from mice subjected to the indicated treatments. Lung tissue was processed and stained using H&E to assess overall tissue morphology, PAS staining to evaluate mucus production, and Masson staining to examine collagen deposition. Black arrows indicate inflammatory cells, mucus, and collagen, respectively. Scale bars, 200 μm (Above). Scale bars, 50 μm (Below). **c**–**f**, Quantification analysis of histological staining in lung sections. (**c**) Airway wall thickness, (**d**) inflammatory cell infiltration, (**e**) mucus production area, and (**f**) collagen content were quantified using ImageJ software. Results are presented as mean ± s.d, $n = 5$ biologically independent mice per group (**c**–**f**). Significant differences were assessed using a one-way ANOVA with Tukey's multiple comparisons test (**c**–**f**). Source data are provided as a Source Data file.

decreases in the counts of these cell types were observed in the Pulmicort, mLuc-iLNP$_{BUD5}$, and mnbTSLP-iLNP$_{BUD0}$ treatment groups (Fig. 6a, b). As anticipated, the Pulmicort, mLuc-iLNP$_{BUD5}$, and mnbTSLP-iLNP$_{BUD0}$ treatment groups exhibited an increase in BALF macrophage content, whereas the mnbTSLP-iLNP$_{BUD5}$ treatment group restored BALF macrophage levels to those comparable to the PBS group (Fig. 6c). ELISA analysis showed that both budesonide monotherapy and mRNA-based nbTSLP monotherapy effectively decreased serum IgE levels and suppressed the production of key pro-inflammatory cytokines in BALF, including TSLP, IL-4, IL-5, IL-13, and IL-6 (Fig. 6d–i). The combination therapy of budesonide and mnbTSLP resulted in the most significant reduction in T_H2 inflammation, likely due to a synergistic anti-inflammatory effect involving nbTSLP's blockade of the upstream cytokine TSLP binding to its receptor complex TSLPR/IL-7R and budesonide-induced downregulation of pro-inflammatory gene transcription[30].

Bronchial challenge tests were performed to assess the effect of mnbTSLP-iLNP$_{BUD5}$ on alleviating AHR, a key indicator of asthma. Two days after the last challenge, the mice's airways were subjected to invasive plethysmography and escalating doses of methacholine to measure airway resistance using the SCIREQ flexiVent system. Compared to healthy mice, which showed no significant increase in airway resistance even at the highest concentration of methacholine (50 mg/mL), asthmatic mice treated with mLuc-iLNP$_{BUD0}$ exhibited a marked increase in elastance and airway resistance at a methacholine concentration as low as 6.25 mg/mL, indicating the onset of an asthmatic response (Fig. 6j, k). Inhalation of all four therapeutic agents reduced the airway response to methacholine stimulation, with mnbTSLP-iLNP$_{BUD5}$ showing the least fluctuation in airway resistance following increased methacholine exposure, suggesting that inhalation of mnbTSLP-iLNP$_{BUD5}$ effectively mitigates the development of AHR. The ability of each group to attenuate the airway response to methacholine stimulation is negatively correlated with their corresponding IL-13 expression levels in BALF (Fig. 6f), a critical cytokine involved in mucus cell hyperplasia and airway remodeling during the pathogenesis of AHR.

Anti-asthmatic effect of inhaled mnbTSLP-iLNP$_{BUD5}$ in steroid-resistant asthmatic mice

We subsequently explored the therapeutic potential of mnbTSLP-iLNP$_{BUD5}$ in a mouse model of steroid-resistant asthma. An 11-week chronic asthma murine model exhibiting steroid resistance was induced by repeated intranasal OVA challenges and further exacerbated by TSLP (Fig. 7a), as previous investigations have confirmed that exogenous TSLP can promote steroid resistance during airway inflammation[9,35]. Figure 7b shows that, upon increased methacholine stimulation, asthmatic mice treated with mLuc-iLNP$_{BUD5}$ and Pulmicort displayed a continuous increase in airway resistance. These results confirm that the treatments had no significant effect on reducing airway resistance, a key parameter of AHR, indicating a steroid-resistant response. A moderate increase in airway resistance was observed in asthmatic mice treated with the subcutaneously administered monoclonal anti-TSLP antibody (Tezepelumab). Unlike other treatments, nebulized mnbTSLP-iLNP$_{BUD0}$ or mnbTSLP-iLNP$_{BUD5}$ allowed asthmatic mice to maintain nearly stable, low airway resistance upon increased methacholine stimulation, indicating a dramatic mitigation of AHR. Notably, nebulized mnbTSLP-iLNP$_{BUD5}$ resulted in the lowest airway resistance, closely resembling the trend observed in the healthy group (Fig. 7b).

Histological examination was next performed on lungs isolated from the indicated groups. H&E, PAS, and Masson staining results revealed that neither Pulmicort nor mLuc-iLNP$_{BUD5}$ effectively treated this specific asthma phenotype, as both failed to reduce inflammatory cell infiltration, airway wall thickening, excessive mucus production, or collagen deposition in the airways (Fig. 7c). Inhaled mnbTSLP-iLNP$_{BUD5}$ demonstrated superior efficacy in inhibiting airway inflammation and remodeling compared to inhaled mnbTSLP or injected Tezepelumab alone, with significant reductions in inflammatory cell percentage, airway wall thickness, mucus production area, and collagen content, achieving results comparable to the healthy group (Fig. 7d–g). Taken together, these results highlight the ability of mnbTSLP-iLNP$_{BUD5}$ to reverse steroid resistance and enhance the anti-asthmatic effect.

Body weight of the mice in each group was monitored throughout the challenging period. As shown in Supplementary Fig. 13, asthmatic mice treated with inhaled Pulmicort and mLuc-iLNP$_{BUD5}$ exhibited persistent weight loss after three inhalations, likely due to metabolic disruption caused by ongoing chronic airway inflammation[36], including excessive inflammatory cell infiltration and mucus hypersecretion. On the other hand, mice treated with Tezepelumab, mnbTSLP-iLNP$_{BUD0}$, or mnbTSLP-iLNP$_{BUD5}$ alone gradually regained body weight, reaching levels similar to those of healthy mice by the final inhalation (Supplementary Fig. 15). This was likely due to the restoration of energy metabolism resulting from the resolution of airway inflammation mediated by anti-TSLP therapies[37].

To further elucidate the mechanisms underlying the effect of mnbTSLP-iLNP$_{BUD5}$ in overcoming steroid resistance, we conducted Western blot analysis to assess the phosphorylation levels of STAT3 and p38 MAPK in lung tissues from mice treated with different conditions. Both p-STAT3 and p-p38 MAPK are known to play critical roles in impairing the translocation of the GR complex to the nucleus, either by directly phosphorylating GR or through disrupting its interactions with nuclear import machinery, thereby inhibiting the anti-inflammatory effects of budesonide[12,13]. Compared to the healthy group, steroid-resistant asthmatic mice receiving treatment of mLuc-iLNP$_{BUD0}$ (negative control) exhibited a significant increase in the levels of p-STAT3 and p-p38 MAPK. Compared to the mLuc-iLNP$_{BUD0}$ group, both the Pulmicort and mLuc-iLNP$_{BUD5}$ treatment groups showed only a modest reduction in p-STAT3 and p-p38 MAPK levels (Fig. 7h and Supplementary Fig. 16). These results aligned with histological findings from both budesonide-based treatment groups, which revealed substantial inflammatory cell infiltration, excessive mucus production, and collagen deposition in the airways (Fig. 7c), indicating that the model is less responsive to budesonide-based therapies. Notably, mnbTSLP-iLNP$_{BUD5}$ treatment significantly reduced p-STAT3 and p-p38 MAPK levels in the lungs of budesonide-resistant asthmatic mice, bringing these levels closer to those observed in the healthy group (Fig. 7h and Supplementary Fig. 14). The combination of mnbTSLP and budesonide showed superior efficacy compared to either mnbTSLP-iLNP$_{BUD0}$ or Tezepelumab alone, as confirmed by histological results (Fig. 7c). The enhanced therapeutic effect of inhaled mnbTSLP-iLNP$_{BUD5}$ in budesonide-resistant asthmatic mice likely stems from its ability to reduce phosphorylation of STAT3 and p38 MAPK, promoting GR complex translocation into the nucleus and restoring sensitivity to budesonide-based therapy[9,38]. Additionally, the suppression of downstream inflammatory mediators, such as IL-6 and TNF-α, induced by mnbTSLP-iLNP$_{BUD5}$ may further contribute to its enhanced anti-asthmatic effects[39].

In vivo safety assessment of mnbTSLP-iLNP$_{BUD5}$

Finally, we administered the same dosing regimen used in the steroid-resistant asthma treatment to healthy mice in order to assess the potential systemic toxicity of mnbTSLP-iLNP$_{BUD5}$. Daily body weight measurements of the mice showed no significant differences between the healthy control group and the groups receiving any treatment (Supplementary Fig. 17). Two days after the final administration, the BALB/c mice were sacrificed, and whole blood, serum, and major organs were collected for routine blood tests, biochemical analysis, and histological examination. No significant changes were observed in creatinine (Cre), blood urea nitrogen (BUN), alanine aminotransferase (ALT), aspartate aminotransferase (AST), white blood cell (WBC)

https://doi.org/10.1038/s41467-025-61114-4

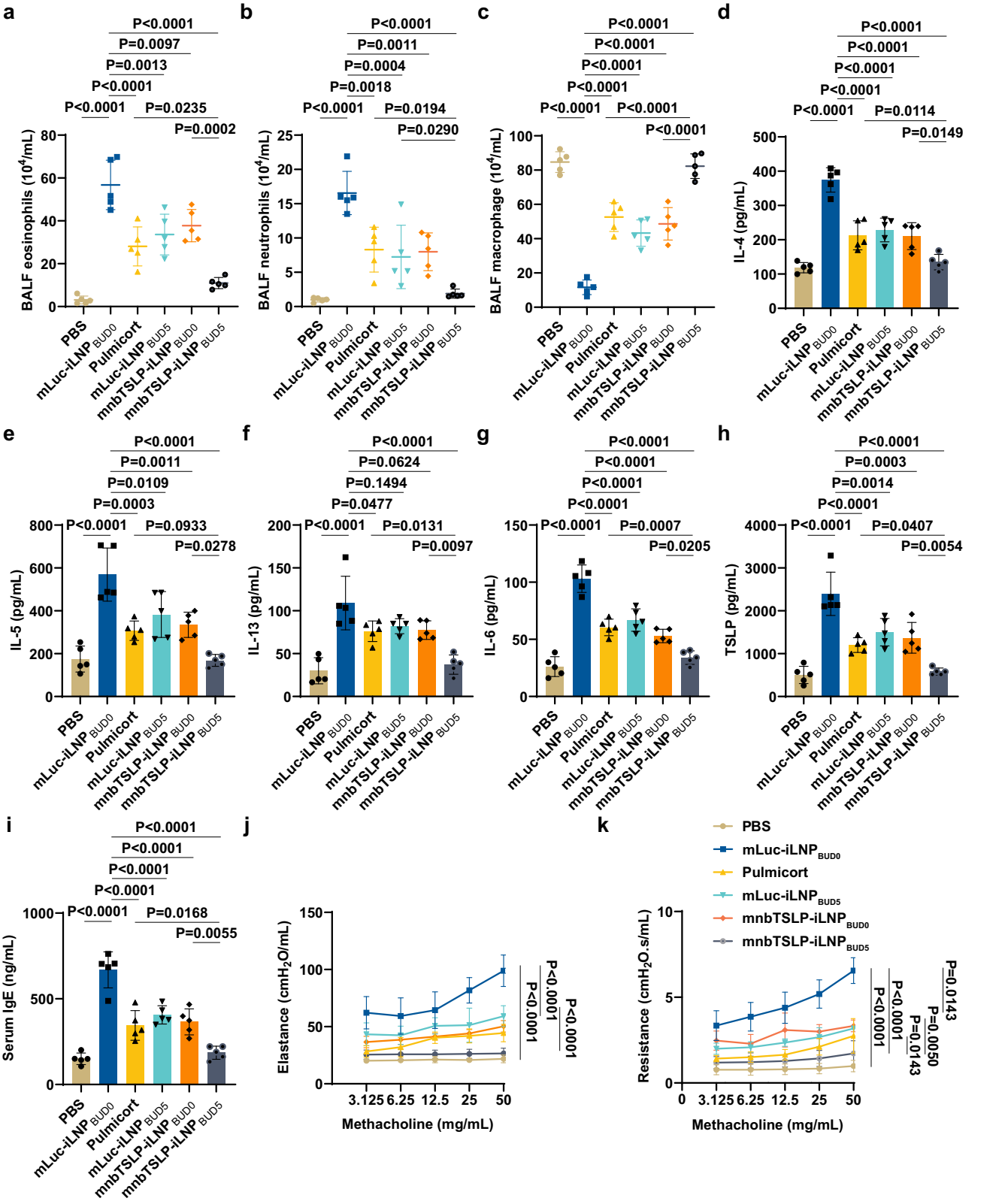

Fig. 6 | Inhalation of mnbTSLP-iLNP$_{BUD5}$ resolves airway inflammation and improves pulmonary function in severe asthmatic mice. a–**c**, Eosinophils (**a**), neutrophils (**b**), and macrophages (**c**) counts in the BALF of mice following the indicated treatments were assessed using a Diff-Quik stain kit. **d**–**h**, ELISA analysis of IL-4 (**d**), IL-5 (**e**), IL-13 (**f**), TSLP (**g**), and IL-6 (**h**) levels in the BALF collected from the mice receiving the indicated treatments. **i** IgE levels in the serum collected from the mice receiving the indicated treatments, determined by ELISA assay. **j, k** The elastance (**j**) and airway resistance (**k**) of the mice subjected to the indicated treatments were assessed using the SCIREQ flexiVent system following stimulation with various concentrations of methacholine. Results are presented as mean ± s.d, $n = 5$ biologically independent mice per group **a**–**k**. Significant differences were assessed using a one-way ANOVA with Tukey's multiple comparisons test **a**–**i** or by Two-way ANOVA with Tukey's multiple comparisons test **j, k**. Source data are provided as a Source Data file.

https://doi.org/10.1038/s41467-025-61114-4

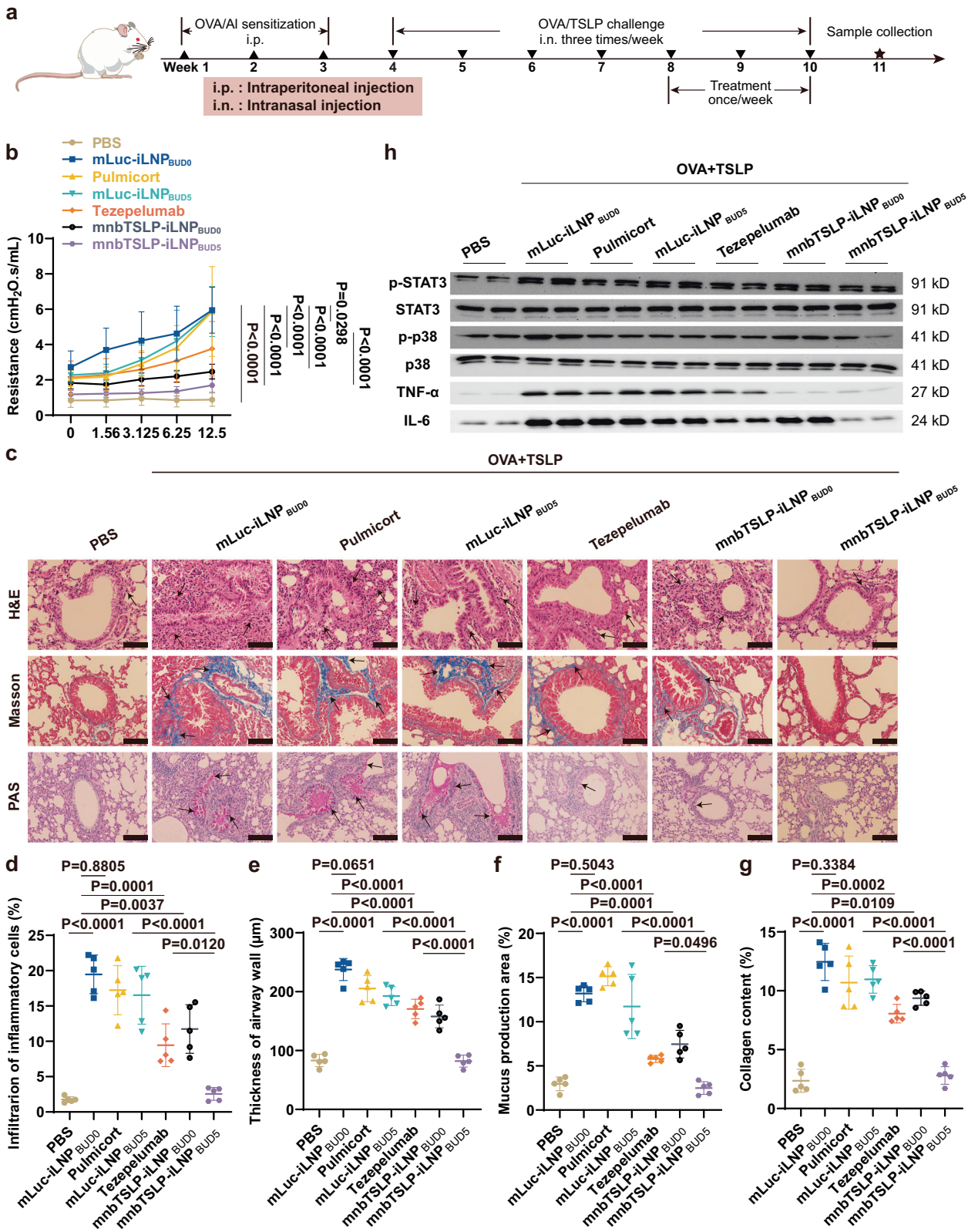

count, red blood cell (RBC) count, hemoglobin (HGB) levels, or hematocrit (HCT) in mice receiving the various treatments (Fig. 8a–h). Furthermore, H&E staining of other major organs, excluding the lungs, showed no evident pathological changes in the cardiac, hepatic, splenic, or renal tissues following inhalation of mnbTSLP-iLNP$_{BUD5}$ or any of the other treatment regimens. (Fig. 8i). Overall, inhaled mnbTSLP-iLNP$_{BUD5}$ demonstrated a highly acceptable safety profile in the non-targeted organs of mice, offering a promising non-invasive nanomedicine approach for treating steroid-resistant asthma.

Discussion

Corticosteroids bind to cytoplasmic GRs, forming a GR complex that translocates to the nucleus and binds to glucocorticoid-responsive elements (GREs)[5]. This process upregulates anti-inflammatory

Fig. 7 | Inhaled mnbTSLP-iLNP$_{BUD5}$ exhibits a synergistic effect in a murine model of OVA/TSLP-induced steroid-resistant asthma. a Schematic illustration of an OVA/TSLP-induced steroid-resistant asthma model and treatment regimen for the specified therapies. **b** Airway resistance of the mice subjected to the indicated treatments were assessed using the SCIREQ flexiVent system following stimulation with various concentrations of methacholine. **c** Representative microscopic images of lung tissue sections stained with H&E, PAS, and Masson stains, with black arrows indicating the presence of inflammatory cells, mucus, and collagen fibers, respectively. Scale bars, 50 μm. **d**–**g**, Quantification analysis of section staining for thickness of airway walls (**d**), infiltration of inflammatory cells (**e**), mucus production area (**f**), and collagen content (**g**), performed using ImageJ software. **h** Western blot analysis of p-p38, total p38, p-STAT3, total STAT3 expression in lung tissue homogenates, as well as the levels of IL-6 and TNF-α in BALF. Lung tissue homogenates and BALF were collected from mice receiving the indicated treatments. Results are presented as mean ± s.d, $n = 5$ biologically independent mice per group (**b, d**–**g**) and $n = 2$ biologically independent samples per group (**h**). Significant differences were assessed using a two-way ANOVA with Tukey's multiple comparisons test (**b**) or by one-way ANOVA with Tukey's multiple comparisons test (**d**–**g**). P values as indicated. Source data are provided as a Source Data file.

cytokines (e.g., TGF-β, IL-10) and downregulates pro-inflammatory cytokines (e.g., IL-1β, IL-6, IL-4, IL-5, IL-13, TNF-α), thereby exerting anti-inflammatory effects[5,6]. Inhaled corticosteroids are commonly used to reduce airway inflammation through these mechanisms, supporting their clinical application in asthma management. However, the nuclear translocation of the GR complex can be impaired by alarmins (TSLP, IL-25, and IL-33) through the overactivation of signaling molecules (e.g., STAT3, MAPK, NF-κB, STAT5)[20,40,41]. This inhibited nuclear uptake of the GR complex in airway epithelial cells may contribute to the development of steroid resistance[12]. Efforts have also focused on developing therapeutic agents that inhibit underlying inflammation and airway remodeling through various molecular mechanisms, including TSLP-specific antibodies, as an alternative treatment for this inadequately controlled disease[4]. TSLP is an epithelial cell-derived cytokine that binds to the TSLPR/IL-7R complex and plays an upstream role in asthma progression[2]. The interaction between TSLP and the TSLPR/IL-7R complex activates Janus kinases (JAK1 and JAK2), which in turn phosphorylate STAT3, MAPKs, NF-κB, and STAT5, thereby influencing transcriptional responses to corticosteroids and simultaneously promoting airway inflammation[38].

Although TSLP-specific antibodies, such as Tezepelumab, have shown therapeutic potential in managing both T_H2 and non-T_H2 asthma, there are several drawbacks associated with systemic antibody delivery, including local adverse effects from subcutaneous injections, allergic reactions due to the immunogenicity of exogenous proteins, suboptimal pulmonary distribution and limited therapeutic efficacy[42,43]. More importantly, TSLP not only plays a crucial role in the progression of asthma but also is involved in multiple physiological processes, including tumor suppression and immune homeostasis, suggesting that systemic blockade of TSLP could inevitably lead to immune dysregulation and other side effects (such as viral infections and promotion of inflammatory disorders)[8,9]. These challenges highlight the need for lung-specific delivery of combination therapeutics to address severe asthma, including steroid-resistant forms, through different mechanisms.

Asthma is a chronic, heterogeneous disease with multiple underlying pathophysiological mechanisms, making single-drug therapy often insufficient to alleviate its diverse symptoms[1,41]. Therefore, developing combination therapies is essential to broaden efficacy across different phenotypes. On the other hand, inhalation is widely considered the optimal route of administration for respiratory diseases like asthma, due to its intrinsic ability to target the lungs, provide prolonged drug retention in lung tissue, and enhance patient tolerability[22,44]. In light of this, we propose a non-invasive, inhalable ASCEND approach that combines mRNA-mediated nanobody therapy with corticosteroid treatment, harnessing their synergistic effects to enhance therapeutic outcomes, including protection against airway remodeling driven by chronic inflammation and immune activation, in the management of severe asthma. This combinatory therapeutic approach involves partially replacing cholesterol with budesonide in the iLNP formulation, owing to their similar steroidal structures and lipophilic properties. In our ASCEND strategy, budesonide serves a dual role as both a carrier for mnbTSLP and an anti-asthmatic drug. The mnbTSLP-encoded nanobody was designed as a dimer of two VHHs connected by a short peptide to enhance its half-life and binding affinity[45]. To facilitate the secretion of nbTSLP from epithelial cells and its subsequent interaction with TSLP, mnbTSLP was constructed by inserting a secretion signal peptide sequence directly upstream of the initiation codon. Western blot analysis identified a protein band at approximately 35 kDa, and ELISA measurements confirmed its efficient binding to TSLP, indicating that the designed mnbTSLP successfully mediated the expression and secretion of the anti-TSLP nanobody. The resulting mRNA-iLNP$_{BUD5}$ demonstrated superior stability during nebulization, as evidenced by minimal fluctuations in DLS measurements, zeta potential, EE, and morphological characteristics, while also retaining its ability to express the corresponding protein. Intriguingly, we found that replacing approximately a quarter of the cholesterol molar proportion with budesonide in the iLNP formulation most effectively improved mRNA transfection efficiency. This effect could be attenuated by the GR inhibitor mifepristone. This finding suggests that incorporating budesonide at an optimal content promotes cellular uptake of mRNA-iLNP$_{BUD5}$, likely due to its interaction with the membrane receptor. It is worth noting that mnbTSLP-iLNP$_{BUD5}$ treatment significantly reduced the mRNA levels of pro-inflammatory factors IL-6, TNF-α, and TSLP in 16HBE cells after LPS stimulation, indicating a potent anti-inflammatory response. Upon nebulization, mnbTSLP-iLNP$_{BUD5}$ was distributed to the lungs and deposited throughout the bronchiolar and alveolar epithelium, enabling localized translation into nbTSLP, as confirmed by Western blot analysis of BALF proteins. The results indicate that mnbTSLP-iLNP$_{BUD5}$ can serve as a "lead drug" for the lung-targeted combinatory delivery of budesonide and mRNA therapeutics.

We then investigated the potential of the mnbTSLP-iLNP$_{BUD5}$-mediated ASCEND approach for asthma management using murine asthma models. Using an OVA-induced acute asthma mouse model, which mirrors the features observed in human asthma[46,47], we found that aerosolized mnbTSLP-iLNP$_{BUD5}$ significantly inhibited the production of pro-inflammatory cytokines, mucus secretion, collagen deposition, and airway wall hypertrophy across all test groups, demonstrating superior protective efficacy against stimulus-induced airway inflammation, AHR, and airway remodeling. We next established a chronic asthma model by intraperitoneally injecting OVA/Alum, followed by intranasal administration of OVA and TSLP, and evaluated the potential of mnbTSLP-iLNP$_{BUD5}$ as a therapeutic option for steroid-resistant asthma. Treatment with either inhaled Pulmicort or mLuc-iLNP$_{BUD5}$ did not reduce airway inflammation or reverse airway remodeling, suggesting the development of steroid resistance in the asthmatic mice. In contrast, despite having a lower budesonide content than Pulmicort, inhalation of mnbTSLP-iLNP$_{BUD5}$ significantly reduced inflammatory cell infiltration, prevented airway structural changes, and maintained low airway resistance during methacholine stimulation in steroid-resistant asthma, by inhibiting the TSLP/STAT3 and TSLP/p38 signaling pathways. These findings suggest therapeutic synergy between budesonide and nbTSLP. Notably, treatment with mnbTSLP-iLNP$_{BUD0}$ demonstrated superior outcomes compared to Tezepelumab alone, suggesting that inhaled delivery of mRNA-based antibody therapy may offer greater efficacy than systemic delivery of monoclonal antibody therapy targeting the same pathway. The

https://doi.org/10.1038/s41467-025-61114-4

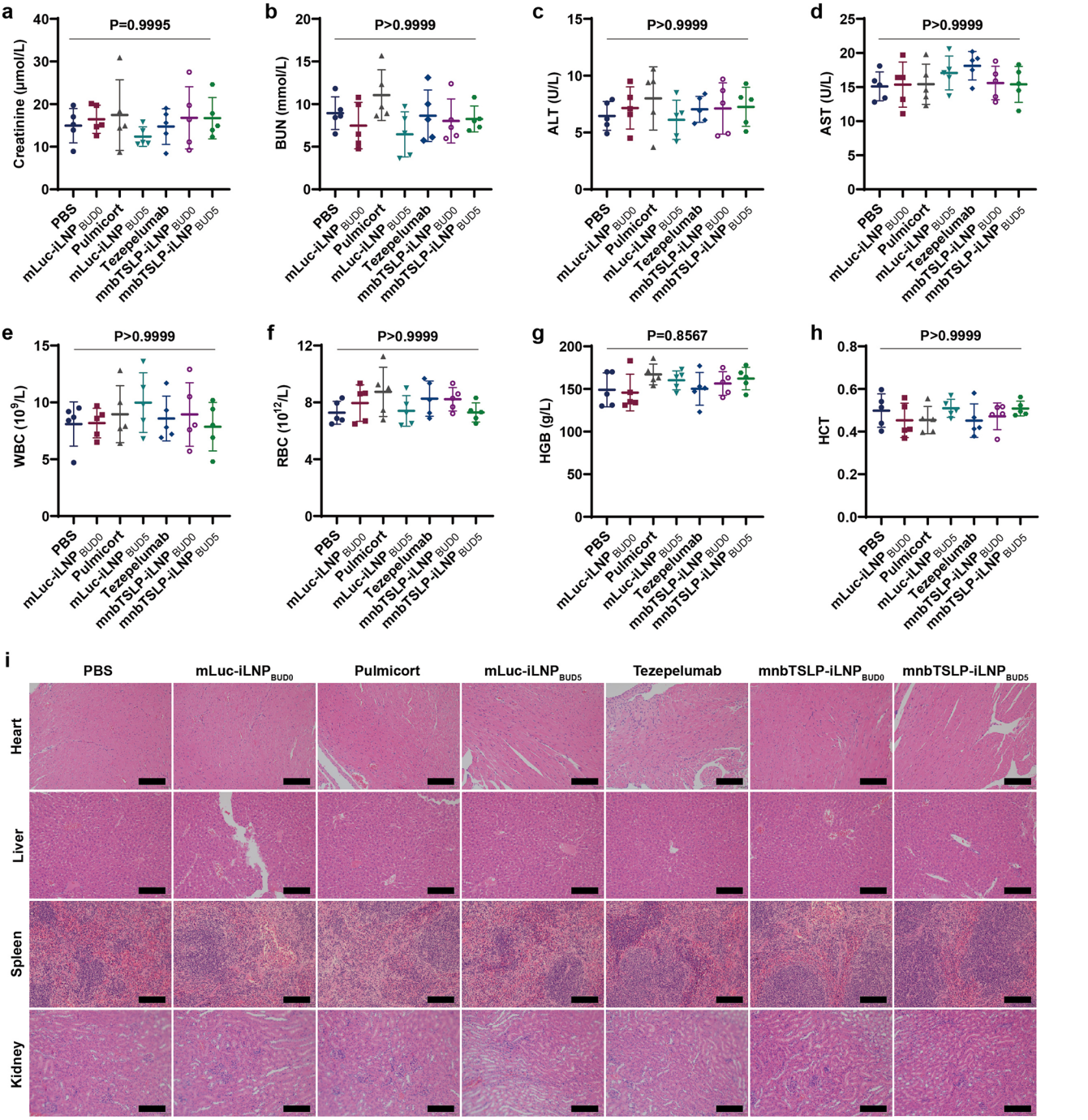

Fig. 8 | In vivo safety assessment of mnbTSLP-iLNP$_{BUD5}$. **a**–**d**, Biochemical analysis of serum Creatinine (**a**), BUN (**b**), ALT (**c**), and AST (**d**) in healthy BALB/c mice following weekly administration of the indicated therapeutics for three weeks. **e**–**h**, Hematological analysis in whole blood samples from healthy bALB/c mice receiving weekly administration of the indicated therapeutics for three weeks, including WBC (**e**), RBC (**f**), HGB (**g**), and HCT (**h**). Results are presented as mean ± s.d, $n = 5$ biologically independent mice per group. Significant differences were assessed using a one-way ANOVA with Tukey's multiple comparisons test (**a**–**h**). P values as indicated. Source data are provided as a Source Data file. (**i**) Representative H&E-stained tissue sections from the heart, liver, spleen, and kidneys of mice treated as indicated. Scale bars, 100 μm.

enhanced anti-inflammatory effect of mnbTSLP-iLNP$_{BUD5}$ in both acute and steroid-resistant asthma models results from the synergistic mechanism between nbTSLP and budesonide, where nbTSLP promotes the translocation of the budesonide-receptor complex to enhance budesonide's local action in suppressing T_H2 inflammation, while also modulating the upstream immune cascade, including the release of IL-6 and TNF-α by DCs and other immune cells[4,10,12]. This underscores the promising therapeutic potential of the ASCEND approach, which enables localized co-delivery of mRNA encoding the anti-TSLP nanobody and the small molecule budesonide via an iLNP platform for the management of severe asthma.

Although our previous research shows promising results, further investigations could be considered for future work. A range of stimuli (e.g., viruses, house dust mites, and cigarette smoke) trigger asthma symptoms through distinct mechanisms and larger animal species (e.g., rats, pigs, and primates), with airway physiology more similar to that of humans, should be used to establish asthma models for evaluating the pharmacological efficacy and biosafety of mnbTSLP-

$iLNP_{BUD5}$ across diverse asthma phenotypes[11,48–50]. For chronic asthma of prolonged duration, circular RNA and other sustained-release technologies can be explored to enable long-term drug release and maintain effective concentrations with a single dose[51–54]. Considering the heterogenicity of asthma, co-encapsulating multiple RNA sequences within a single iLNP might maximize the inhibition of asthma attacks by targeting various signaling pathways involved in asthma development. Despite these limitations, ASCEND-optimized iLNP simultaneously targets multiple inflammatory pathways, aiming to address steroid-resistant asthma with greater efficiency and improved patient compliance compared to monotherapy with Pulmicort or Tezepelumab.

In conclusion, this study primarily focuses on developing an ASCEND approach that enables lung-targeted co-delivery of budesonide and an mRNA-encoded anti-TSLP nanobody, and evaluating its synergistic therapeutic effects in both the OVA-induced acute asthma mouse model and the OVA/TSLP-induced steroid-resistant asthma mouse model as a proof of concept. To the best of our knowledge, LNP-assisted inhaled delivery of a combination of mRNA and small compounds has rarely been explored for the management of severe asthma. The developed ASCEND approach not only opens a new avenue for treating steroid-resistant asthma but also provides a robust iLNP platform for the simultaneous, lung-targeted delivery of nucleic acid therapeutics targeting multiple pathways, along with steroidal compounds for the treatment of other respiratory diseases.

Methods

Key resources

The ionizable lipid AA3-DLin was synthesized using an enzyme-catalyzed one-step method[26]. We purchased the complementary lipid components (DSPC, cholesterol, and DMG-PEG2000) from AVT Pharmaceutical Tech Co., Ltd., and acquired all qRT-PCR primers (see sequences in Supplementary Table 3) from Suzhou Genewiz Biotechnology Co., Ltd. Supplementary Table 4 lists all other key resources (mRNA, antibodies, commercial kits, and reagents).

Cell culture

HEK293T cell was acquired from ATCC. 16HBE and BEAS-2B cells were generously furnished by Zhongshan Hospital, Fudan University. Both 16HBE and BEAS-2B cells were commonly used human respiratory epithelial cell lines. HEK293T and BEAS-2B cells were cultured in Dulbecco's Modified Eagle Medium (DMEM), whereas 16HBE cells were maintained in Roswell Park Memorial Institute (RPMI) 1640 medium. All cell lines were propagated in their respective media, supplemented with 10% FBS and 1% penicillin-streptomycin. The culture was conducted in an incubator with a thermostatic setting of 37 °C, under humidified conditions containing 5% CO_2.

Animals

The female BALB/c mice, aged 6-8 weeks, used in all in vivo experiments were sourced from Shanghai Lingchang Biotechnology Co., Ltd. All mice were housed in pathogen-free facilities at Shanghai Jiao Tong University (Shanghai, China). Mice were housed under controlled conditions (12 h light/dark cycle, 25 °C ambient temperature, 50% humidity) with ad libitum access to food and water. All animal experiments were approved by the Institutional Animal Care and Use Committee of Shanghai Jiao Tong University (Ethical approval number: A2023178-002).

Preparation and nebulization of iLNP

The iLNPs were prepared following the protocol described in previous literature[21]. Specifically, cationic lipid (AA3-DLin or ALC-0315), DSPC, cholesterol, budesonide, and DMG-PEG2000 were mixed in the specified ratio (Supplimentary Table 5) and dissolved in anhydrous ethanol to a final concentration of 10 mg/mL to form the lipid phase. Meanwhile, the aqueous phases were prepared by introducing mLuc, mEGFP, $mRNA^{Cy5}$ or mnbTSLP into a citrate buffer (50 mM, pH 4.0), maintaining a constant weight ratio of mRNA to ionizable lipid at 1:15. A microfluidic device (Aitesen, China) was then utilized to mix the aqueous phase with the lipid phase at a fixed volume ratio of 3:1, ensuring rapid integration. The resulting mixtures were incubated at room temperature or 4 °C for 20 min to facilitate complete encapsulation of mRNA within the lipid nanoparticle core, yielding homogeneous nanoparticles. The nanoparticles were then dialyzed against PBS (pH 7.4) or Tris buffer (pH 7.0) for 4–6 h using dialysis cassettes (3.5 K MWCO, Thermo Fisher Scientific, USA) to eliminate any unconjugated substances.

For nebulization, the LNPs were concentrated to an mRNA concentration of 0.2–0.3 μg/μL by centrifugation at 2465 × *g* for 30 min, then adjusted to 0.1 μg/μL mRNA by dilution with poloxamer 188 (8 mg/mL) in HEPES buffer (25 mM, pH 6.0). The resulting solution was then added drop by drop into the vibrating mesh nebulizer (Aerogen® Solo, Ireland), and the iLNP aerosols were collected.

Physicochemical characterization of iLNP before and after nebulization

The zeta potential, PDI, particle size, and size distribution of the iLNP or iLNP aerosol were analyzed using a ZetaSizer Nano ZSE (Malvern, UK), both before and after nebulization. iLNP or its aerosol was diluted in HEPES buffer for the above analysis. The morphology of the LNPs was examined using Cryo-TEM (Thermo Fisher Scientific, USA). The encapsulation efficiency of mRNA was determined using the Quant-iT™ RiboGreen RNA Assay Kit following the provided instructions.

In vitro transfection efficiency of nebulized iLNPs

To assess the in vitro transfection efficiency of nebulized iLNPs, BEAS-2B cells were seeded at a density of 1×10^5 cells per well in a 24-well plate and cultured overnight to allow for exponential growth. When the cells reached 80–90% confluence, various nebulized iLNPs containing a fixed dose of 0.5 μg of mEGFP were introduced, with the cells cultured in a serum-free medium. Six hours later, the iLNPs were removed, and the cells were washed with sterile PBS. Fluorescence images of EGFP-positive cells were captured using an inverted fluorescence microscope (IX73, Olympus, Japan). After imaging, the cells were detached using Trypsin-EDTA, resuspended in PBS, and centrifuged to obtain single-cell suspensions. The suspensions were then analyzed on a BD LSR II flow cytometer (BD Biosciences, USA), and EGFP-positive cells were quantified using FlowJo v10 software.

Bioluminescence study

$mLuc\text{-}iLNP_{BUD0}$, $mLuc\text{-}iLNP_{BUD5}$, $mLuc\text{-}iLNP_{BUD9.5}$, $mLuc\text{-}iLNP_{BUD14}$, $mLuc\text{-}iLNP_{BUD19}$, $mLuc\text{-}iLNP^{ALC\text{-}0315}{}_{BUD0}$, and $mLuc\text{-}iLNP^{ALC\text{-}0315}{}_{BUD5}$ were administered via inhalation to BALB/c mice, with each mouse receiving 15 μg of mLuc. Six hours following the administration, 200 μL of 15 mg/mL D-Luciferin potassium salt solution was injected intraperitoneally into each mouse. Five minutes after the injection, the mice were sacrificed, and their major organs (hearts, livers, spleens, lungs, and kidneys) were harvested and imaged for bioluminescence using the IVIS Spectrum instrument (PerkinElmer, USA). Signal intensity in the lungs was quantified using Living Image v4 software.

Assessment of storage stability

The storage stability of $mEGFP\text{-}iLNP_{BUD5}$ was evaluated at 4 °C. On days 0, 1, 7, 14, and 30, the size distribution of $mEGFP\text{-}iLNP_{BUD5}$ was determined using a ZetaSizer Nano ZSE (Malvern, UK).

Analysis of serum stability

To assess the serum stability of nebulized $mEGFP\text{-}iLNP_{BUD5}$, the formulation was incubated in PBS containing 10% FBS at two different pH values (7.4 and 6.8) for 24 h at 37 °C. At specified time points, samples

were collected, and particle size was measured using a ZetaSizer Nano ZSE (Malvern, UK) after appropriate dilution with the corresponding buffer solution.

Physicochemical properties and bioactivities of mEGFP-iLNP$_{BUD5}$ under various storage conditions

To further evaluate the impact of storage conditions on the mRNA delivery efficiency of iLNP$_{BUD5}$, we stored both mEGFP-iLNP$_{BUD5}$ (with or without the 5 wt% sucrose) and mLuc-iLNP$_{BUD5}$ (with or without the 5 wt% sucrose) at 4 °C or 20 °C for 30 days. The physicochemical properties, such as particle size and PDI, of the specified iLNPs were determined both before and after nebulization using a ZetaSizer Nano ZSE (Malvern, UK). In vitro and in vivo transfection efficiencies were analyzed using the BD LSR II flow cytometer (BD Biosciences, USA) and the IVIS Spectrum instrument (PerkinElmer, USA), respectively.

Validation of in vitro mucus penetration assay

The artificial mucus was prepared by dissolving DNA (10 mg/mL), mucin (5 mg/mL), sterile egg yolk lotion (0.5%, v/v), DTPA (5.9 μg/mL), NaCl (5 mg/mL), KCl (2.2 mg/mL), and RPMI (2%, v/v) in water. A 10% (w/v) heating-dissolved gelatin solution was added to a 24-well plate, and the specified volume of artificial mucus was introduced onto the surface of the gelatin ladder after it had solidified at room temperature. We applied naked mRNA^{Cy5} and mRNA^{Cy5}-iLNP$_{BUD5}$ to the upper surface of the artificial mucus. At designated time points, the artificial mucus was discarded, followed by PBS washing and gelatin dissolution via heating. The fluorescence intensity in the gelatin layer was measured using a microplate reader (Tecan, Switzerland).

Lysosomal escape

16HBE cells were seeded in confocal dishes and allowed to grow for 24 h. They were then treated with nebulized mRNA^{Cy5}-iLNP$_{BUD5}$ in serum-free culture medium. At specified time intervals (0.5, 2, and 4 h), the nebulized mRNA^{Cy5}-iLNP$_{BUD5}$ was removed, and the cells were thoroughly rinsed three times with PBS to remove any uninternalized particles. The cells were then stained with LysoTracker Green for 30 min to label the lysosomes, followed by three rinses with PBS to remove any excess stain. To visualize nuclear DNA, the cells were treated with Hoechst 33342 for 10 min. Finally, mRNA^{Cy5}-iLNP$_{BUD5}$ escape from the lysosomes was documented using a Leica STELLARIS 5 LSCM (Leica, Germany). The Pearson's colocalization values at different time points were calculated using ImageJ software.

Analysis of EGFP expression efficiency in nebulized EGFP-iLNP$_{BUD5}$

16HBE cells were plated in confocal dishes and cultured for 24 h. They were then treated with nebulized mRNA-iLNP$_{BUD5}$ for an additional 24 h, followed by the removal of uninternalized particles. To visualize nuclear DNA, the cells were stained with Hoechst 33342 for 10 min. EGFP-positive regions were subsequently captured using a Leica STELLARIS 5 LSCM (Leica, Germany).

Structural and functional integrity analysis of mnbTSLP

Naked mnbTSLP or mnbTSLP-iLNP$_{BUD5}$ was incubated individually with 10% FBS at 37 °C for a specified period. Following incubation, a terminal concentration of 2% (v/v) Triton X-100 solution was added to disrupt the LNP structure, thereby releasing the encapsulated mnbTSLP from mnbTSLP-iLNP$_{BUD5}$. A 2% agarose gel was then cast, and both naked mnbTSLP and mnbTSLP extracted from mnbTSLP-iLNP$_{BUD5}$ were mixed with 1× nucleic acid loading buffer. Electrophoresis was performed at 110 V for 10 min, with 10 μL of each sample loaded into separate wells. The resulting gel was analyzed using a ChemiDoc imaging system (Bio-Rad, USA) to assess the integrity of mnbTSLP.

Concurrently, 1 μg of naked mnbTSLP with lipo3000 or mnbTSLP-iLNP$_{BUD5}$ at various time intervals was transfected into BEAS-2B cells. After 6 h of incubation, the cell supernatant and lysate were collected for Western blot analysis, which was then performed using a Chemi-Doc imaging system (Bio-Rad, USA) to quantify protein expression levels and assess the protective effect of mnbTSLP-iLNP$_{BUD5}$ on mnbTSLP translation.

Expression and purification of nbTSLP

mnbTSLP was transfected into HEK293T cells using lipo3000 to achieve sufficient expression of mnbTSLP. After a three-day incubation, the supernatant was harvested, centrifuged, and concentrated using centrifugal filters (Millipore) with a 10 kDa molecular weight cutoff at 3220 × *g*. Leveraging the interaction between the His-Tag and the nickel column (QIAGEN, Germany), the concentrated product was purified through a two-step nickel column chromatography process, with nbTSLP eluted using an imidazole gradient at varying concentrations. The purity of the resulting mnbTSLP was evaluated by Coomassie bright blue staining and Western blot analysis.

Binding affinity analysis

The binding affinity between nbTSLP and TSLP was assessed using an ELISA assay. A 96-well microplate (Greiner) was coated with 100 μL of recombinant TSLP protein (1 ng/μL) in PBS and incubated at 4 °C for 24 h. After aspirating the coating solution, non-specific binding was blocked with 2% BSA in PBS at 37 °C for 60 min. The wells were washed five times with PBST, and excess moisture was removed. Purified nbTSLP concentrations were determined using the BCA assay, and serial dilutions (1600 ng/mL to 0.195 ng/mL) in PBS with 1% BSA were prepared. Aliquots (100 μL) of each dilution were added to the wells and incubated at 37 °C for 2 h. After washing, 100 μL of anti-Flag-Tag antibody (1:5000 dilution) was added and incubated for 60 min at 37 °C. Following washing, 100 μL of Goat anti-mouse IgG HRP (1:5000 dilution) was added, and the wells were incubated for 1 h. Then, 100 μL of TMB substrate was added, and the reaction was incubated in the dark for 15 min at 37 °C. The reaction was stopped with 100 μL of 2 M H_2SO_4, and absorbance was measured at 450 nm using a microplate reader (Tecan, Switzerland).

In vitro efficacy study of an LPS-induced inflammatory 16HBE cell model

16HBE cells were seeded at 1×10^5 cells per well in a 24-well plate and incubated overnight at 37 °C with 5% CO_2. The next day, the medium was replaced with serum-free RPMI 1640 to synchronize the cells. To optimize LPS stimulation, cells were treated with increasing LPS concentrations (0.1–100 μg/mL) for 4 h. For time optimization, cells were exposed to 10 μg/mL LPS for 4, 12, or 24 h. After treatment, cells were washed with PBS, collected, resuspended, and lysed using Trizol for total RNA extraction. IL-6 mRNA expression levels were quantified using a Real-Time PCR Detection System (Bio-Rad, USA) to assess inflammation. Following this, an inflammatory model of 16HBE cells was established by treating them with a specific concentration of LPS for the indicated time. mnbTSLP-iLNP$_{BUD5}$ was then introduced to the inflammatory 16HBE cells and incubated for 24 h. The mRNA expression levels of IL-6, TNF-α, and TSLP were quantified by qRT-PCR to assess the therapeutic efficacy of mnbTSLP-iLNP$_{BUD5}$.

Cell viability assay

16HBE cells were seeded in a 96-well plate at a density of 1×10^4 cells per well and incubated overnight. The following day, the cells were treated with various concentrations of mnbTSLP-iLNP$_{BUD5}$ for 24 h. After treatment, the culture medium was aspirated, and each well was replenished with serum-free medium containing 10 μL of CCK-8 solution. The plate was incubated at 37 °C for an additional 2 h to allow colorimetric development. Finally, the absorbance at 450 nm was

measured using a microplate reader (Tecan, Switzerland) to assess cell viability or proliferation.

Biodistribution, lung deposition, and cellular uptake of nebulized mnbTSLP-iLNP$^{Cy5}_{BUD5}$

To monitor the lung deposition of mnbTSLP-iLNP$_{BUD5}$, a modified iLNP formulation (mnbTSLP-iLNP$^{Cy5}_{BUD5}$) was prepared by substituting 30% of the cholesterol with Cy5-labeled cholesterol. BALB/c mice were administered a single dose of mnbTSLP-iLNP$^{Cy5}_{BUD5}$ using a vibrating mesh nebulizer (Aerogen® Solo, Ireland). Twenty-four hours post-nebulization, the mice were euthanized, and major organs were harvested for fluorescence imaging using the IVIS system (PerkinElmer, USA). The lungs were fixed, dehydrated, and embedded in optimal cutting temperature (OCT) compound. Lung samples were sectioned into 10 μm-thick slices and counterstained with DAPI to highlight cell nuclei. LSCM was used to visualize mnbTSLP-iLNP$^{Cy5}_{BUD5}$ deposition in the lungs, bronchi, and alveoli.

To evaluate in vivo cellular uptake of mnbTSLP-iLNP$_{BUD5}$ in pulmonary cell subtypes, OVA-induced asthmatic mice were administered mnbTSLP-iLNP$^{Cy5}_{BUD5}$ via inhalation. Six hours post-administration, the mice were euthanized, and their lungs were excised. The harvested lung tissues were mechanically dissociated into fragments and enzymatically digested at 37 °C for 60 min using a 1 × PBS solution supplemented with collagenase I (5 mg/mL), collagenase IV (2 mg/mL), hyaluronidase (500 μg/mL), and HEPES (0.5 M). The resulting single-cell suspension was sequentially filtered through a 40 μm cell strainer and treated with red blood cell lysis buffer for 5 min. After centrifugation at 201 × *g* for 3 min, the pelleted cells were washed twice with ice-cold PBS and subjected to viability staining using Zombie Aqua™ dye for 10 min at 4 °C. To minimize nonspecific antibody binding, cells were pre-treated with an Fc blocker in staining buffer for 15 min. Subsequently, multiparametric surface staining was performed by incubating the cells on ice for 30 min with the following fluorochrome-conjugated antibodies: anti-CD31 (endothelial cells), anti-CD45 (immune cells), and anti-EpCAM (epithelial cells). Following two additional washes, cells were resuspended in the cell staining buffer. Quantitative analysis of mnbTSLP-iLNP$^{Cy5}_{BUD5}$ uptake across distinct lung cell populations was conducted using a BD LSRFortessa™ flow cytometer (BD Biosciences, USA), with gating strategies based on forward/side scatter properties and lineage-specific marker expression.

High performance liquid chromatography assay

The incorporation efficiency of budesonide within the LNP structure was assessed using high-performance liquid chromatography (HPLC) with an analytical method previously described[55]. Given the lipophilic nature of budesonide and the aqueous solubility of mRNA, the mnbTSLP-iLNP$_{BUD5}$ nanostructure was disrupted by adding 300 μL of HPLC-grade methanol to 100 μL of the LNP suspension, which facilitated the separation of mRNA from the lipid components. The mixture was then centrifuged at 2465 × g for 5 min, and the resulting sediment was removed. A lipid solution containing budesonide was obtained and prepared for HPLC injection (Agilent 1260 II, China). A standard curve was generated by serially diluting the budesonide standard in the mobile phase to create a concentration range from 0.25 μg/mL to 100 μg/mL. The chromatographic conditions were as follows: column, Agilent XDB-C_{18}, 5 μm, 250 mm × 4.6 mm; mobile phase, methanol/water (7:3, v/v); flow rate, 1 mL/min; injection volume, 20 μL; and detection wavelength, 254 nm.

Establishment and administration of an acute asthma mouse model

On days 1, 7, and 14, female BALB/c mice (6–8 weeks old) were sensitized with intraperitoneal injection of 100 μg OVA absorbed onto 1 mg Alum. From days 21 to 27, the immunized mice were challenged intranasally with 50 μg OVA daily. To assess the therapeutic effects of the treatments, each group was administered an inhalation of either mLuc-iLNP$_{BUD0}$ (30 μg mLuc), Pulmicort (40 μg budesonide), mLuc-iLNP$_{BUD5}$ (40 μg budesonide), mnbTSLP-iLNP$_{BUD0}$ (30 μg mnbTSLP), or mnbTSLP-iLNP$_{BUD5}$ (30 μg mnbTSLP) 6 h prior to each OVA challenge. Healthy mice receiving an equivalent volume of PBS were used as the control group.

Chronic asthma model and administration

On day 1, female BALB/c mice (6–8 weeks old) received an intraperitoneal injection of 100 μg OVA and 1 mg Alum, followed by booster injections on day 7 and 14. Nasal challenges were performed on day 21, with exposure to 20 μg OVA combined with 10 μg TSLP three times per week, on alternate days during 7 weeks (from day 21 to day 70). Inhalation administration of mLuc-iLNP$_{BUD0}$, Pulmicort, mLuc-iLNP$_{BUD5}$, mnbTSLP-iLNP$_{BUD0}$, or mnbTSLP-iLNP$_{BUD5}$ began on day 56 and continued through day 70, 2 h after the final weekly challenge. The dosages of iLNPs and Pulmicort were based on those used in acute asthma therapy. Tezepelumab was administered intravenously via the tail vein at a dose of 70 μg on the same time as the other therapeutic treatments. Healthy mice receiving an equivalent volume of PBS were used as the control group.

Collection of BALF

Forty-eight hours after the final allergen challenge, the mice in the acute asthma model were anesthetized, and bronchoalveolar lavage was performed. The lungs were first flushed with 1 mL of ice-cold, sterile PBS containing 100 μM EDTA, administered via a tracheal catheter with a 1 mL syringe. The resulting bronchoalveolar lavage fluid (BALF) was centrifuged at 2465 × *g* for 5 min at 4 °C to collect the cellular pellet, which was retained for Diff-Quik staining. A second lavage was then performed using 0.75 mL of ice-cold, sterile PBS. The supernatant from the lavage was carefully collected, aliquoted, and stored at −80 °C for subsequent cytokine quantification.

Cell differential analysis in BALF using Diff-Quik staining

The cell pellets derived from BALF were resuspended in 1 mL of 1% BSA in PBS, and the concentration was determined using a hemocytometer. To analyze the immune cell types in BALF, cells were adjusted to the desired concentration, migrated onto a slide, and stained with Diff-Quik staining solution according to the manufacturer's instructions. Eosinophils, neutrophils, and macrophages were identified based on their morphology and counted under a microscope (Olympus, Japan).

BALF cytokine measurements

The BALF supernatant was diluted to the specified concentration. TSLP, IL-4, IL-5, IL-6, and IL-13 levels in BALF from mice treated with mLuc-iLNP$_{BUD0}$, Pulmicort, mLuc-iLNP$_{BUD5}$, mnbTSLP-iLNP$_{BUD0}$, mnbTSLP-iLNP$_{BUD5}$, or PBS were measured using ELISA kits, in accordance with the manufacturer's instructions.

IgE measurements

Serum IgE concentrations were measured using a mouse IgE ELISA kit, following the manufacturer's protocol. For serum collection, blood was obtained by ocular enucleation after alveolar lavage or lung function assessments. The blood was then centrifuged twice to separate the serum, which was used for ELISA analysis.

Histological analysis

Mice were euthanized 48 h after the final OVA or OVA/TSLP challenge. The lungs were isolated and fixed in 4% paraformaldehyde for histological analysis. Paraffin-embedded 5 μm sections of the left lobe were stained with hematoxylin and eosin (H&E), Masson's trichrome (Masson), and periodic acid-Schiff (PAS) using commercial staining kits. H&E staining was used to assess airway inflammation and wall thickness, Masson staining to evaluate collagen deposition around the

airways, and PAS staining to examine goblet cell hyperplasia and mucus secretion. Images were captured at various magnifications using a BX53 upright fluorescence microscope (Olympus, Japan).

Measurements of airway hyperresponsiveness

Mice were deeply anesthetized 48 h after the final OVA or OVA/TSLP challenge with tribromoethanol in saline (600 mg/kg) to suppress spontaneous respiration. A tracheotomy was then performed, and the trachea was intubated with a stainless-steel catheter, which was connected to the SCIREQ FlexiVent system (Montreal, QC, Canada) to assess lung function. Methacholine (0–50 mg/mL) was nebulized at increasing concentrations using an ultrasonic nebulizer integrated with the SCIREQ FlexiVent system, following the manufacturer's protocol, once baseline readings had stabilized. After a deep inflation, lung function measurements were recorded and are presented as the maximum resistance values corresponding to the escalating doses of methacholine.

In vivo biosafety evaluation

To assess the potential in vivo toxicity of mnbTSLP-iLNP$_{BUD5}$, a three-week mouse model of administration was developed. Healthy female BALB/c mice (6–8 weeks old) were administered weekly with the same dosage of therapeutic components used in the chronic asthma experiments. Body weights of mice were recorded weekly. Two days after the final administration, approximately 100 μL of whole blood was collected from each mouse via retro-orbital puncture into an anticoagulant tube for the measurement of RBCs, WBCs, HGB, and HCT. Additionally, the remaining whole blood was centrifuged twice at 2465 × *g* for 15 min at 4 °C to obtain serum, with the supernatant collected for the analysis of creatinine, BUN, ALT, and AST. Ultimately, the mice were sacrificed, and their hearts, livers, spleens, and kidneys were harvested for H&E staining to assess tissue morphology and potential toxicity.

qRT-PCR analysis

BEAS-2B cells were lysed with Trizol reagent and incubated at room temperature for 5 min. Chloroform was added, and the mixture was shaken vigorously. The mixture was left at room temperature to separate into phases. After centrifugation, the upper aqueous phase was collected, and isopropanol was added to precipitate the RNA. The solution was mixed gently and incubated at room temperature before centrifuging again to collect the RNA. The RNA pellet was washed with 95% ethanol, air-dried, and resuspended in DEPC-treated water. RNA purity and concentration were assessed by measuring the A260/A280 ratio using a microplate UV-Vis spectrophotometer (Thermo Fisher Scientific, USA). Total RNA was then reverse transcribed to synthesize complementary DNA. qPCR analysis was conducted using a six-channel fluorescence-based qPCR instrument (Bio-Rad, USA). Gene-specific primers and the fluorescent dye SYBR Green were used to quantify the mRNA expression levels of target inflammatory cytokines, including IL-6, TSLP, and TNF-α, relative to the endogenous control gene glyceraldehyde-3-phosphate dehydrogenase (GAPDH). Relative quantification was achieved by calculating cycle threshold (Ct) values and applying the $2^{-\Delta\Delta Ct}$ method.

Western blot analysis

16HBE cells and mouse lung tissue homogenates were lysed using cold RIPA lysis buffer supplemented with 1× protease inhibitor cocktail, and the supernatant was centrifuged to remove sediments. Protein concentrations were determined using a BCA Protein Quantification Kit. The samples were mixed with 5× protein loading buffer at a 4:1 (v/v) ratio, boiled for 5 min, and loaded onto a 10% SDS-PAGE gel for electrophoresis. Proteins were transferred to a polyvinylidene difluoride (PVDF) membrane (Millipore), which was blocked with 5% skimmed milk in TBST for 1 h at room temperature. The PVDF membrane was gently shaken and incubated overnight at 4 °C with the following primary antibodies: mouse anti-His-Tag (1:5000), mouse anti-Flag-Tag (1:5000), mouse anti-β-actin (1:20000), mouse anti-GAPDH (1:50000), mouse anti-STAT3 (1:1000), rabbit anti-p-STAT3 (1:2000), rabbit anti-p38 (1:2000), or rabbit anti-p-p38 (1:10,000). After incubation, the membrane was washed three times with Tris-buffered saline Tween 20 (TBST) for 5 min each. Horseradish peroxidase (HRP)-conjugated anti-mouse antibody (1:5000) or HRP-conjugated goat anti-rabbit IgG (1:5000) was then applied for 1 h at room temperature. Finally, proteins on PVDF membrane were visualized using a chemiluminescence substrate and a chemiDoc imaging system (Bio-Rad, USA) following three additional washes in TBST. The uncropped and unprocessed scans of the blots have been provided in the Source Data file and Supplementary Information file.

Statistical information

All statistical analyses were conducted using GraphPad Prism 8.0.2 software. Results are as mean ± standard deviation (s.d.). For multiple comparisons, one-way or two-way ANOVA with Tukey's multiple comparisons test was used. Exact P values are indicated in the figures, with statistical significance set at $P < 0.05$.

Reporting summary

Further information on research design is available in the Nature Portfolio Reporting Summary linked to this article.

Data availability

All data supporting the conclusions of this study are available within the article and its Supplementary Information files. Source data are provided with this paper. Source data for Figs. 2, 3, 4, 5, 6, 7, and 8, as well as Supplementary Figs. 3, 4, 5, 7, 9, 10, 12, 13, 15, 16, and 17, are provided in the associated source data file. Source data for Supplementary Figs. 8 and 14 are supplied at the end of the Supplementary Information file. Source data are provided with this paper.

References

1. Porsbjerg, C. et al. Asthma. *Lancet* **401**, 858–873 (2023).
2. Lambrecht, B. & Hammad, H. The immunology of asthma. *Nat. Immunol.* **16**, 45–56 (2015).
3. van der Ploeg, E. K. et al. Type-2 CD8+ T-cell formation relies on interleukin-33 and is linked to asthma exacerbations. *Nat. Commun.* **14**, 5137 (2023).
4. Pelaia, G., Vatrella, A. & Maselli, R. The potential of biologics for the treatment of asthma. *Nat. Rev. Drug Discov.* **11**, 958–972 (2012).
5. Weikum, E. et al. Glucocorticoid receptor control of transcription: precision and plasticity via allostery. *Nat. Rev. Mol. Cell Biol.* **18**, 159–174 (2017).
6. Cain, D. & Cidlowski, J. Immune regulation by glucocorticoids. *Nat. Rev. Immunol.* **17**, 233–247 (2017).
7. Campa, C. C. et al. Inhalation of the prodrug PI3K inhibitor CL27c improves lung function in asthma and fibrosis. *Nat. Commun.* **9**, 5232 (2018).
8. Verstraete, K. et al. Structure and antagonism of the receptor complex mediated by human TSLP in allergy and asthma. *Nat. Commun.* **8**, 14937 (2017).
9. Ebina-Shibuya, R. & Leonard, W. J. Role of thymic stromal lymphopoietin in allergy and beyond. *Nat. Rev. Immunol.* **23**, 24–37 (2023).
10. Hammad, H. & Lambrecht, B. Dendritic cells and epithelial cells: linking innate and adaptive immunity in asthma. *Nat. Rev. Immunol.* **8**, 193–204 (2008).
11. Zhang, H. et al. Cullin5 drives experimental asthma exacerbations by modulating alveolar macrophage antiviral immunity. *Nat. Commun.* **15**, 252 (2024).
12. Caramori, G., Nucera, F., Mumby, S., Lo Bello, F. & Adcock, I. M. Corticosteroid resistance in asthma: cellular and molecular mechanisms. *Mol. Asp. Med.* **85**, 100969 (2022).

13. Lea, S. et al. P38 MAPK and glucocorticoid receptor crosstalk in bronchial epithelial cells. *J. Mol. Med.* **98**, 361–374 (2020).
14. Kolkhir, P. et al. Type 2 chronic inflammatory diseases: targets, therapies and unmet needs. *Nat. Rev. Drug Discov.* **22**, 743–767 (2023).
15. Agache, I. et al. Efficacy and safety of treatment with biologicals (benralizumab, dupilumab, mepolizumab, omalizumab and reslizumab) for severe eosinophilic asthma: a systematic review for the EAACI Guidelines—recommendations on the use of biologicals in severe asthma. *Allergy* **75**, 1023–1042 (2020).
16. Qin, S. et al. mRNA-based therapeutics: powerful and versatile tools to combat diseases. *Signal Transduct. Target. Ther.* **7**, 166 (2022).
17. Sahin, U., Karikó, K. & Türeci, Ö. mRNA-based therapeutics—developing a new class of drugs. *Nat. Rev. Drug Discov.* **13**, 759–780 (2014).
18. Szefler, S. J. & Eigen, H. Budesonide inhalation suspension: a nebulized corticosteroid for persistent asthma. *J. Allergy Clin. Immunol.* **109**, 730–742 (2002).
19. Kim, H., DeKruyff, R. & Umetsu, D. The many paths to asthma: phenotype shaped by innate and adaptive immunity. *Nat. Immunol.* **11**, 577–584 (2010).
20. Athari, S. S. Targeting cell signaling in allergic asthma. *Signal Transduct. Target. Ther.* **4**, 45 (2019).
21. Bai, X. et al. Optimized inhaled LNP formulation for enhanced treatment of idiopathic pulmonary fibrosis via mRNA-mediated antibody therapy. *Nat. Commun.* **15**, 6844 (2024).
22. Bai, X. et al. Inhaled siRNA nanoparticles targeting IL11 inhibit lung fibrosis and improve pulmonary function post-bleomycin challenge. *Sci. Adv.* **8**, eabn7162 (2022).
23. Bandi, N. & Kompella, U. B. Budesonide reduces vascular endothelial growth factor secretion and expression in airway (Calu-1) and alveolar (A549) epithelial cells. *Eur. J. Pharmacol.* **425**, 109–116 (2001).
24. Chivers, J. E. et al. Differential effects of RU486 reveal distinct mechanisms for glucocorticoid repression of prostaglandin E release. *Eur. J. Biochem.* **271**, 4042–4052 (2004).
25. Corsini, E. et al. Corticosteroids modulate the expression of the PKC-anchoring protein RACK-1 and cytokine release in THP-1 cells. *Pharmacol. Res.* **81**, 10–16 (2014).
26. Li, Z. et al. Enzyme-catalyzed one-step synthesis of ionizable cationic lipids for lipid nanoparticle-based mRNA COVID-19 vaccines. *ACS Nano* **16**, 18936–18950 (2022).
27. Mauger, D. M. et al. mRNA structure regulates protein expression through changes in functional half-life. *Proc. Natl Acad. Sci. USA* **116**, 24075–24083 (2019).
28. Jiang, A. Y. et al. Combinatorial development of nebulized mRNA delivery formulations for the lungs. *Nat. Nanotechnol.* **19**, 364–375 (2024).
29. Sokol, C. et al. A mechanism for the initiation of allergen-induced T helper type 2 responses. *Nat. Immunol.* **9**, 310–318 (2008).
30. Watson, B. & Gauvreau, G. M. Thymic stromal lymphopoietin: a central regulator of allergic asthma. *Expert Opin. Ther. Targets* **18**, 771–785 (2014).
31. Liu, S. et al. Charge-assisted stabilization of lipid nanoparticles enables inhaled mRNA delivery for mucosal vaccination. *Nat. Commun.* **15**, 9471 (2024).
32. Li, H. et al. Single-cell transcriptomic analysis reveals key immune cell phenotypes in the lungs of patients with asthma exacerbation. *J. Allergy Clin. Immunol.* **147**, 941–954 (2021).
33. Han, S. et al. Distinctive CD39+CD9+ lung interstitial macrophages suppress IL-23/Th17-mediated neutrophilic asthma by inhibiting NETosis. *Nat. Commun.* **15**, 8628 (2024).
34. Hewitt, R. J. & Lloyd, C. M. Regulation of immune responses by the airway epithelial cell landscape. *Nat. Rev. Immunol.* **21**, 347–362 (2021).
35. Kabata, H. et al. Thymic stromal lymphopoietin induces corticosteroid resistance in natural helper cells during airway inflammation. *Nat. Commun.* **4**, 2675 (2013).
36. Kachroo, P. et al. Metabolomic profiling reveals extensive adrenal suppression due to inhaled corticosteroid therapy in asthma. *Nat. Med.* **28**, 814–822 (2022).
37. Cho, R. et al. Thymic stromal lymphopoietin induces adipose loss through sebum hypersecretion. *Science* **373**, eabd2893 (2021).
38. Matera, M. G., Rogliani, P., Calzetta, L. & Cazzola, M. TSLP inhibitors for asthma: current status and future prospects. *Drugs* **80**, 449–458 (2020).
39. Zheng, D., Liwinski, T. & Elinav, E. Inflammasome activation and regulation: toward a better understanding of complex mechanisms. *Cell Discov.* **6**, 36 (2020).
40. Saglani, S. et al. IL-33 promotes airway remodeling in pediatric patients with severe steroid-resistant asthma. *J. Allergy Clin. Immunol.* **132**, 676–685.e13 (2013).
41. Vannella, K. M. et al. Combinatorial targeting of TSLP, IL-25, and IL-33 in type 2 cytokine-driven inflammation and fibrosis. *Sci. Transl. Med.* **8**, 337ra65 (2016).
42. Hoy, S. M. Tezepelumab: first approval. *Drugs* **82**, 461–468 (2022).
43. O'Byrne, P. M. et al. Development of an inhaled anti-TSLP therapy for asthma. *Pulm. Pharmacol. Ther.* **78**, 102184 (2023).
44. Patton, J. & Byron, P. Inhaling medicines: delivering drugs to the body through the lungs. *Nat. Rev. Drug Discov.* **6**, 67–74 (2007).
45. Ma, L. et al. Preclinical development of a long-acting trivalent bispecific nanobody targeting IL-5 for the treatment of eosinophilic asthma. *Respir. Res.* **23**, 316 (2022).
46. Mazarakis, N. et al. Investigation of molecular mechanisms of experimental compounds in murine models of chronic allergic airways disease using synchrotron Fourier-transform infrared microspectroscopy. *Sci. Rep.* **10**, 11713 (2020).
47. Zhang, H. et al. AMFR drives allergic asthma development by promoting alveolar macrophage-derived GM-CSF production. *J. Exp. Med.* **219**, e20211828 (2022).
48. Quan, J. et al. Epithelial SIRT6 governs IL-17A pathogenicity and drives allergic airway inflammation and remodeling. *Nat. Commun.* **14**, 8525 (2023).
49. Boulet, L. P. et al. Smoking and asthma: clinical and radiologic features, lung function, and airway inflammation. *Chest* **129**, 661–668 (2006).
50. Woodrow, J. S. et al. Asthma: the use of animal models and their translational utility. *Cells* **12**, 1091 (2023).
51. Jin, G. et al. A single infusion of engineered long-lived and multifunctional T cells confers durable remission of asthma in mice. *Nat. Immunol.* **25**, 1059–1072 (2024).
52. Wu, S. et al. A single dose of an adenovirus-vectored vaccine provides protection against SARS-CoV-2 challenge. *Nat. Commun.* **11**, 4081 (2020).
53. Chen, H. et al. Chemical and topological design of multicapped mRNA and capped circular RNA to augment translation. *Nature Biotechnology* https://doi.org/10.1038/s41587-024-02393-y (2024).
54. Zhu, P. et al. IL-13 secreted by ILC2s promotes the self-renewal of intestinal stem cells through circular RNA circPan3. *Nat. Immunol.* **20**, 183–194 (2019).
55. Liu, Y. et al. Localized myocardial anti-inflammatory effects of temperature-sensitive budesonide nanoparticles during radiofrequency catheter ablation. *Research* **2022**, 9816234 (2022).

Acknowledgments

The work was funded by the National Key Research and Development Program of China (2023YFC2606003), "Open Competition to Select the Best Candidates" Key Technology Program for Nucleic Acid Drugs of NCTIB (grant no. NCTIB2022HS02002), the Natural Science Foundation of Shanghai (23ZR1427600), and the Program of Shanghai Frontiers

Science Center of Drug Target Identification and Delivery (ZXWH2170101). X.X. acknowledges support from the National Science Foundation (2001606) and the Gustavus and Louise Pfeiffer Research Foundation Award.

Author contributions

J.H., X.X., and X.-Q.Z. originated the study and devised the experiments. J.H. conducted most experiments and drafted the original manuscript. X.B. contributed to protein purification and in vivo experiments. J.H., X.B., W.S., X.X., and X.-Q.Z. analyzed and discussed the results. X.X. and X.-Q.Z. supervised the research and revised and refined the manuscript.

Competing interests

The authors declare no competing interests.

Additional information

Supplementary information The online version contains supplementary material available at https://doi.org/10.1038/s41467-025-61114-4.

Correspondence and requests for materials should be addressed to Xiaoyang Xu or Xue-Qing Zhang.

Peer review information *Nature Communications* thanks Yizhou Dong and the other, anonymous, reviewers for their contribution to the peer review of this work. A peer review file is available.